



UNIVERSITY OF LEEDS

This is a repository copy of *Automated seismic waveform location using Multichannel Coherency Migration (MCM)--II. Application to induced and volcano-tectonic seismicity.*

White Rose Research Online URL for this paper:  
<http://eprints.whiterose.ac.uk/139227/>

Version: Accepted Version

---

**Article:**

Shi, P [orcid.org/0000-0001-5782-245X](https://orcid.org/0000-0001-5782-245X), Nowacki, A [orcid.org/0000-0001-7669-7383](https://orcid.org/0000-0001-7669-7383), Rost, S [orcid.org/0000-0003-0218-247X](https://orcid.org/0000-0003-0218-247X) et al. (1 more author) (2019) Automated seismic waveform location using Multichannel Coherency Migration (MCM)--II. Application to induced and volcano-tectonic seismicity. *Geophysical Journal International*, 216 (3). pp. 1608-1632. ISSN 0956-540X

<https://doi.org/10.1093/gji/ggy507>

---

© The Author(s) 2018. Published by Oxford University Press on behalf of The Royal Astronomical Society. This is a pre-copyedited, author-produced PDF of an article accepted for publication in *Geophysical Journal International* following peer review. The version of record: Shi, P , Nowacki, A, Rost, S et al. (1 more author) (Accepted: 2018) Automated seismic waveform location using Multichannel Coherency Migration (MCM)--II. Application to induced and volcano-tectonic seismicity. *Geophysical Journal International*. ISSN 0956-540X (In Press) is available online at: <https://doi.org/10.1093/gji/ggy507>. Uploaded in accordance with the publisher's self-archiving policy.

**Reuse**

Items deposited in White Rose Research Online are protected by copyright, with all rights reserved unless indicated otherwise. They may be downloaded and/or printed for private study, or other acts as permitted by national copyright laws. The publisher or other rights holders may allow further reproduction and re-use of the full text version. This is indicated by the licence information on the White Rose Research Online record for the item.

**Takedown**

If you consider content in White Rose Research Online to be in breach of UK law, please notify us by emailing [eprints@whiterose.ac.uk](mailto:eprints@whiterose.ac.uk) including the URL of the record and the reason for the withdrawal request.



[eprints@whiterose.ac.uk](mailto:eprints@whiterose.ac.uk)  
<https://eprints.whiterose.ac.uk/>

# 1 **Automated seismic waveform location using Multichannel** 2 **Coherency Migration (MCM)–II. Application to induced and** 3 **volcano-tectonic seismicity**

4 Peidong Shi,<sup>1\*</sup> Andy Nowacki,<sup>1</sup> Sebastian Rost<sup>1</sup> and Doug Angus<sup>2</sup>

<sup>1</sup> *School of Earth and Environment, University of Leeds, Leeds, LS2 9JT, UK*

<sup>2</sup> *ESG Solutions, Kingston, ON K7K 7K2, Canada*

5 Received 2018 \*\*\*\* \*\*; in original form 2017 October 20

## 6 **SUMMARY**

7 Locating microseismic events is essential for many areas of seismology including volcano and  
8 earthquake monitoring and reservoir engineering. Due to the large number of microseismic  
9 events in these settings, an automated seismic location method is required to perform real time  
10 seismic monitoring. The measurement environment requires a precise and noise-resistant event  
11 location method for seismic monitoring. In this paper, we apply Multichannel Coherency Mi-  
12 gration (MCM) to automatically locate microseismic events of induced and volcano-tectonic  
13 seismicity using sparse and irregular monitoring arrays. Compared to other migration-based  
14 methods, in spite of the often sparse and irregular distribution of the monitoring arrays, the  
15 MCM can show better location performance and obtain more consistent location results with  
16 the catalogue obtained by manual picking. Our MCM method successfully locates many trig-  
17 gered volcano-tectonic events with local magnitude smaller than 0, which demonstrates its  
18 applicability on locating very small earthquakes. Our synthetic event location example at a  
19 carbon capture and storage site shows that continuous and coherent drilling noise in industrial  
20 settings will pose great challenges for source imaging. However, automatic quality control  
21 techniques including filtering in the frequency domain and weighting are used to automati-  
22 cally select high quality data, and can thus effectively reduce the effects of continuous drilling

23 noise and improve source imaging quality. The location performance of the MCM method for  
24 synthetic and real microseismic datasets demonstrates that the MCM method can perform as a  
25 reliable and automatic seismic waveform analysis tool to locate microseismic events.

26 **Key words:** Earthquake source observations – computational seismology – time-series anal-  
27 ysis – earthquake monitoring and test-ban treaty verification.

## 28 1 INTRODUCTION

29 Microseismic or passive seismic monitoring has been used extensively in monitoring geo-industrial  
30 applications (e.g., hydraulic fracturing, carbon dioxide storage and mining setting (Power et al.  
31 1976; Verdon et al. 2011; Gibowicz & Kijko 2013; Shi et al. 2018a)) as well as hazard monitor-  
32 ing (e.g., volcano-seismology and slope stability (Wilks et al. 2017; Xu et al. 2011)). As a cost-  
33 effective monitoring technique, microseismic monitoring is used to demonstrate storage security  
34 of carbon capture and storage (CCS) (Verdon et al. 2010; Shi et al. 2018c). It is also an effective  
35 method for monitoring volcanoes and forecasting potential eruptions (McNutt 1996; Lavallée et al.  
36 2008). Microseismic monitoring can provide geomechanical deformation information induced by  
37 fluid injection or flow, which can be used to evaluate rock failure processes in the reservoir of a  
38 carbon storage site or volcanic edifice.

39 Noise is an inevitable feature of recorded seismic data. Typically, random noise is assumed  
40 to be stationary with a Gaussian distribution, whereas real noise is often non-stationary and so  
41 does not conform to a single Gaussian distribution (Birnie et al. 2016; Yuan et al. 2018b). With  
42 these features, seismic data with real noise are often more challenging for seismic processing and  
43 more difficult to deal with than Gaussian or white noise. For CCS, microseismic monitoring is  
44 often conducted during carbon dioxide injection. Therefore, the ambient noise due to the fluid  
45 flow and injection exists all the time during the injection process, especially for monitoring arrays  
46 which are deployed close to the injection well. Local drilling with associated continuous drilling  
47 noise can also affect the recorded seismic data significantly. The injection and drilling noise are

\* Corresponding author: Peidong Shi. Email: eepsh@leeds.ac.uk. Fax: +44 113 343 5259

48 continuous and are often coherent across many of the receivers. They can form a great challenge  
49 for microseismic event location in CCS (Barkved et al. 2002; Knudsen et al. 2006; Birnie et al.  
50 2016, 2017). Therefore, suitable ways to reduce or remove real noise and obtaining accurate event  
51 location results are required.

52 For CCS and volcano seismicity, a large number of seismic events can happen within a short  
53 period, which can be very difficult and time-consuming to locate by manual arrival time picking  
54 (Yuan et al. 2018a). In addition, the ever increasing monitoring data volume and larger monitoring  
55 arrays also put great demands on automatic seismic location algorithms for efficient microseismic  
56 monitoring. The traditional arrival time based location methods require phase identification and  
57 picking, thus are not suitable for automatic event location. Although there are ways to perform an  
58 automatic arrival time picking (Bai & Kennett 2000; Maggi et al. 2009), manual picking is still  
59 required to increase the picking reliability when the signal-to-noise ratio of seismic data is low or  
60 the arrivals of seismic events are overlapped. There have been various migration-based location  
61 methods developed to automatically locate seismic events using recorded waveforms (Kao & Shan  
62 2007; Gharti et al. 2010; Drew et al. 2013; Grigoli et al. 2013a,b; Zhebel & Eisner 2014; Langet  
63 et al. 2014; Cesca & Grigoli 2015; Grigoli et al. 2016). Compared with arrival time based methods  
64 where the arrival times are determined by manual picking, automated waveform based location  
65 methods do not need phase picking and association, thus are more efficient and have the ability to  
66 identify more seismic events. Small, more numerous seismic events which cannot be picked man-  
67 ually or automatically can be effectively identified by fully utilizing the recorded full waveforms.  
68 Thus the automated waveform based location methods can help add more insights into the frac-  
69 turing process and natural earthquakes. By using the waveforms and the matched filter technique,  
70 Peng & Zhao (2009) detected a large number of missing aftershocks along the Parkfield section of  
71 the San Andreas fault and used the newly detected seismic events to understand the postseismic  
72 deformation around the rupture zone associated with the mainshock of the 2004 Parkfield earth-  
73 quake. However, the matched filter technique requires reliable waveform templates. Therefore,  
74 this technique is not suitable for research areas where there is no available event catalogue.

75 Migration-based methods have the potential to be applied as real time location schemes, yet

76 the location reliability and accuracy of these methods is often unsatisfactory in presence of strong  
77 noise. Location accuracy is very important in terms of correctly imaging the fracture process and  
78 geometry, which can be used to reveal the source mechanism and deformation orientation. Large  
79 location errors during microseismic monitoring of CCS and volcano seismicity may contribute to  
80 huge economic loss or larger risk as the injection may be terminated prematurely if the induced  
81 fracture length has been exaggerated or volcano activity is underestimated because of mislocation  
82 of volcano seismicity. The other problem which often challenges migration-based location meth-  
83 ods is the station coverage and distribution. Sparse monitoring stations hinder the utilization of  
84 waveform coherency for migration-based location methods, which causes poor noise-resistance  
85 and location performance. Irregular station distribution will reduce imaging resolution and lead to  
86 blurred location results. However, due to the restrictions of the actual deployment environment and  
87 cost, practical monitoring arrays are often sparse and irregularly distributed especially for natural  
88 earthquake monitoring arrays. Therefore, an automatic and precise seismic location method which  
89 can work on sparse and irregular monitoring arrays as well as efficiently with dense and/or regular  
90 networks is in great demand.

91 Shi et al. (2018b) proposed a fully automated seismic location method based on waveform  
92 coherency. This automated location method utilizes Multichannel Coherency Migration (MCM)  
93 and is suitable for locating induced seismicity and natural earthquakes. Different to traditional  
94 migration-based location methods which locate the source by stacking waveforms of characteristic  
95 functions, MCM calculates the multichannel coherency among stations and stacks the coherency to  
96 reveal the source location and origin time. By utilizing multichannel waveform coherency, MCM  
97 exhibited excellent location performance with high resolution and outstanding noise resistance.  
98 The multichannel coherency has also been utilized to improve the horizontal imaging resolution  
99 in seismic interpretation (Yuan et al. 2017). Compared to traditional migration-based location  
100 methods, MCM can extract more effective information from seismic waveforms, which give it the  
101 ability to locate microseismic and resist interference with noise and other non-related events. The  
102 theory and synthetic tests of the multidimensional MCM event-location method can be found in  
103 Shi et al. (2018b). Here, we demonstrate that the MCM location method can be used to automati-

104 cally locate both injection induced and volcano-tectonic microseismic events especially when the  
 105 monitoring array is sparse and/or irregularly distributed. We also compare and discuss the loca-  
 106 tion results with other commonly used migration methods under different real noise levels using  
 107 sparse and irregular monitoring arrays. First, as a feasibility study, we use the MCM to locate two  
 108 volcano-tectonic earthquakes at the Uturuncu Volcano in Bolivia using a sparse monitoring array  
 109 and also compare the location results with published event locations in the catalogue. We then  
 110 apply the MCM to automatically locate triggered earthquakes following the  $M_w$  8.8 Maule earth-  
 111 quake at Uturuncu (Jay et al. 2012) using four hours of continuous waveform data. Then, synthetic  
 112 seismic data of an irregularly distributed monitoring array with real drilling noise were used to  
 113 evaluate the location performance of different methods for induced seismicity. In order to obtain a  
 114 satisfactory location result, quality control methods to remove the coherent drilling noise are ex-  
 115 plored and discussed. Finally, location performance and imaging resolution in different directions  
 116 of different migration-based methods are analysed and discussed in detail.

## 117 2 THEORY AND COMPUTATIONAL EFFICIENCY ANALYSIS

118 In this section, we will briefly introduce the 2-dimensional MCM (for a more detailed description  
 119 and the multidimensional MCM see Shi et al. (2018b)). For MCM, at a particular imaging point  
 120  $k$  and origin time  $t_0$ , the correlation coefficient between the waveforms of two different stations is  
 121 calculated by:

$$122 \quad r_{ij} = \frac{\sum_{t=t_0}^{t_0+t_w} \left[ d_i(t + t_{ki}) - \overline{d_i(t + t_{ki})} \right] \left[ d_j(t + t_{kj}) - \overline{d_j(t + t_{kj})} \right]}{(N_t - 1) \sigma_i \sigma_j}, \quad (1)$$

123 where  $r_{ij}$  is the correlation coefficient (i.e. coherency) between the waveforms at station  $i$  and  $j$ ,  
 124  $d_i$  and  $d_j$  are the two input waveforms within the selected time window for station  $i$  and  $j$ ,  $t_w$  is the  
 125 coherency analysis time window for a particular seismic phase,  $N_t$  is the number of time samples  
 126 in the time window,  $t_{ki}$  and  $t_{kj}$  are traveltimes of a particular seismic phase from imaging point  
 127  $k$  to the station  $i$  and  $j$ ,  $\sigma$  is the standard deviation of the corresponding signal and the overlines  
 128 denote averages.

129 After calculating correlation coefficients for all possible station pairs, the stacking function can

be expressed as

$$p(x, y, z, t_0) = \frac{1}{N(N-1)} \left( \sum_{i<j}^N |r_{ij}^P| + \sum_{i<j}^N |r_{ij}^S| \right). \quad (2)$$

where  $r_{ij}^P$  and  $r_{ij}^S$  represent the waveform coherency of P- and S-phases for station pair  $ij$ ,  $N$  is the number of stations and the number of unique receiver pairs equals  $N(N-1)/2$ ,  $p(x, y, z, t_0)$  is the final 4D imaging function and stores the stacked waveform coherency at position  $(x, y, z)$  and origin time  $t_0$  (Shi et al. 2018b).

The 4D migration volume contains all the information about source location and origin time. Locations  $(x_s, y_s, z_s)$  and origin times  $t_{0s}$  of seismic events can be identified by finding the maximum value above a preset coherency threshold within certain time periods

$$p(x_s, y_s, z_s, t_{0s}) = \max_{t_0 \in [t_1, t_2]} \{p(x, y, z, t_0) \geq p_c\}. \quad (3)$$

As an automated seismic location method, only a few input parameters, i.e. length of coherency analysis time window  $t_w$  and coherency threshold  $p_c$ , are required for MCM in an event location process. The length of coherency analysis time window  $t_w$  should be equal to or larger than the approximate period of seismic phases (Shi et al. 2018b). A longer time window is suggested in order to suppress the interference of noise and other incoherent phases when seismic data contain strong noise or coda waves. The coherency threshold  $p_c$  is determined according to the background noise level. A higher coherency threshold can help identify seismic events which have more probability to be real seismic events, but will also decrease the number of identified seismic events. It is worth noting that the migration process and the event identification process are two totally independent processes. So it is easy to adaptively adjust the coherency threshold according to a migration volume and choose a suitable threshold which can fulfil the requirements of the application.

For event locations based on manual picking, the computational efforts depend on the number of earthquake events in the time period. The more events there are, the more expensive it is to pick and locate them. However, for MCM, the computational cost is independent of the number of events. The computational cost is only related to the number of imaging points, the number of searched origin times and the number of stations. The whole MCM procedure is highly parallelizable, and the migration process is quite independent on different scales (from imaging point

level to origin time level). Therefore, parallel computing in MCM can be performed on different  
 imaging points or different origin times according to actual requirements. Very little communica-  
 tion is required for MCM when performing parallel computations, e.g. maximum migration values  
 of different origin times when performing parallel computing on different origin times or migra-  
 tion values of different imaging points when performing parallel computing on different imaging  
 points. We implement MCM using the Message Passing Interface (MPI) and analyse its compu-  
 tational efficiency on a high performance cluster (Figure 1). Both P- and S-waves are used in the  
 MCM calculation and the number of time samples within the P/S time window is 100. Figure 1 (a)  
 shows the computational times for different numbers of imaging points ( $N_s$ ) and origin times ( $N_t$ )  
 used in the MCM. As can be seen in the figure, the computational cost increases linearly with the  
 number of imaging points and origin times, which demonstrates that the MCM workload scales  
 essentially perfectly. Figure 1 (b) shows the computational times for different numbers of stations  
 ( $N$ ) used in the MCM. As we can see in the figure, the computational cost increases rapidly with  
 the number of stations. Actually, the computational cost is proportional to the number of unique  
 station groups:  $N \times (N - 1)/2$  (as Figure 1 (b) blue line shows), which is in accordance with the  
 theory of MCM (Shi et al. 2018b). Figure 1 (c) shows the computational times and speedup ratios  
 when different numbers of computing cores ( $N_c$ ) are used. As expected the computational times  
 (black line) decrease dramatically when more cores are used in the computation. The speedup  
 ratios (blue line) are calculated by dividing the computational times of different cores by the com-  
 putational time of a single core. Due to the high scalability of the MCM process, the speedup ratio  
 of MCM is very close to the theoretical speedup ratio (red dashed line). Accordingly, we assume  
 that the computational time is proportional to the number of imaging points, the number of origin  
 times and the number of unique station pairs, and the speedup ratio equals the theoretical speedup  
 ratio. Therefore, the computational time  $t = k \times N_s \times N_t \times N \times (N - 1)/N_c$ , where  $k$  is a co-  
 efficient related to computer architecture. Using the data of Figure 1 (a-c), we obtain a coefficient  
 of  $k = 1.5 \times 10^{-7}$  second with the current settings. If real time processing is required, the MCM  
 calculation time should be less than the length of the data. Here, we assume that the sampling in-  
 terval for searched origin times is 0.1 second, and thus we have 10 origin times to process for each



185 second of recorded seismic data. Therefore, for a real time processing, the required cores should  
186 fulfil  $N_c \geq 10 \times k \times N_s \times N \times (N - 1)$ . Figure 1 (d) shows the required cores for real time  
187 processing when different numbers of stations and imaging points are used in MCM. The real time  
188 processing is expensive, but is still feasible with the current computer resources when the number  
189 of stations is not very large (e.g.  $N_s \leq 40$ ). For sparse surface monitoring arrays, the number of  
190 deployed stations is usually smaller than 20. The number of imaging points can be reduced to less  
191 than 300K when locating seismic events in a small region. Therefore, real time processing is com-  
192 pletely feasible in this situation. For example, for the Uturuncu dataset which we will discuss in  
193 detail in the next section, 68 cores are needed to conduct real time processing (shown as the red dot  
194 in Figure 1 (d)). Here, we only implement MCM using CPUs and MPI. Because the whole MCM  
195 process is highly parallelizable and the computation of MCM can be simultaneously processed in  
196 large blocks of data, we anticipate much larger speedup ratios when using Graphics Processing  
197 Units (GPU), which we are currently exploring.

### 198 **3 LOCATION OF SHALLOW SEISMICITY AT UTURUNCU VOLCANO**

199 Uturuncu is a long-dormant stratovolcano in Bolivia, which has an elevation of about 6000 m (Jay  
200 et al. 2012). Recent studies of surface deformation, fumarolic activity and the earthquake rate of  
201 Uturuncu show signs of unrest and potential of eruption again, which calls for close monitoring  
202 (Pritchard & Simons 2004; Sparks et al. 2008; Jay et al. 2012). As shown in Figure 2, 15 three-  
203 component seismometers have been temporarily deployed surrounding the inflating Uturuncu from  
204 April 2009 to April 2010 (Pritchard 2009). The farthest station is located about 25 km from the  
205 volcano summit. The seismometers have a sampling rate of 50 samples/s, which means the highest  
206 effective frequency of the recorded data is 25 Hz. Nine seismometers are short-period instruments  
207 and six seismometers are intermediate-period instruments. The tectonic setting of Uturuncu and  
208 the catalogue for these events located by manual picking can be found in Jay et al. (2012). We  
209 apply the MCM on the recorded continuous waveform data to show the potential of this method in  
210 a volcano-tectonic settings, using a sparse seismic network common in such environments.

### 3.1 Locating two local volcano-tectonic microearthquakes

First, we apply four different waveform migration methods to locate two local volcano-tectonic earthquakes at the Uturuncu and compare the location results. The magnitudes of these two local volcano-tectonic earthquakes are below  $M_L$  1.0. The depths of the two shallow volcano-tectonic earthquakes are above the sea level. We use four different waveform migration techniques, i.e. envelope (Kao & Shan 2007; Gharti et al. 2010), STA/LTA (Drew et al. 2013; Grigoli et al. 2013b), kurtosis (Langet et al. 2014) and MCM (Shi et al. 2018b), to compare the performance in this setting. For STA/LTA migration, the short-term time window has been chosen to be 4 seconds and the long-term time window is 40 seconds. The time window for calculating kurtosis is 4 s. For MCM, a coherent analysis time window of 6 s and a two-channel based coherency scheme are used to locate the seismic events. The coherency threshold of MCM is set to 0.13. Because the monitoring array is very sparse, we set the weighting factors of all stations to 1, which means each trace is equally treated and used for migration. The spatial and temporal intervals used in the source imaging are 100 m and 0.08 s respectively. Because the vertical component data show distinct arrivals of P-waves, we only utilize the direct P-wave to conduct MCM for the vertical component data. Similarly for the north-south and east-west components, we only utilize the direct S-wave to image the events. The coherency of the three component data are then added together to obtain the final imaging values of a particular origin time and space point. The location results of the migration methods are compared to the locations in the catalogue. The velocity model used in the event location is the same layered model as described in Jay et al. (2012).

Figure 3(a) shows the recorded three-component waveforms at station UTCA for the first event, whose local magnitude  $M_L$  is 0.63 (Jay et al. 2012). The direct P-wave and S-wave of this event are distinguishable in the recorded waveforms, but the waveforms contain extended coda. The whole waveform train containing direct waves and coda waves for this event is about 6 seconds. Figure 4 shows the vertical and horizontal profiles of the migration results for the four different waveform migration methods using all available data. The depth (Z-axis) is measured relative to the sea level. The layer at depth 0.5 km which shows a velocity increase can be seen clearly in the migration profiles. The catalogue location (Jay et al. 2012) of this event is displayed as a star in

239 the figure for comparison. For the envelope and STA/LTA migration, the source energy is not well  
240 focused. Thus the event location results of these two methods are not reliable, probably because the  
241 envelope and STA/LTA cannot identify the event onset from the recorded waveforms. For kurtosis  
242 and MCM, the source energy is well focused, thus the location results are more useful. The event  
243 location result of the MCM shows better agreement to the location in the catalogue. The location  
244 deviations of the MCM result relative to the event in the catalogue are 0.584, 0.557 and 0.469 km  
245 in the X, Y and Z directions, respectively (Table 1). Figure 5(a) shows the stacking function of  
246 the MCM method at the position of the most coherent point. The stacking function jumps to the  
247 maximum value at about one coherent analysis time window earlier than the published origin time  
248 of the event and drops down to the noise level quickly. The estimated origin time of the MCM  
249 method can be determined from the maximum coherency time, the analysis time window and the  
250 period of the direct waves. This is in agreement with Shi et al. (2018b). We will discuss this later  
251 in detail in the discussion section. The maximum coherency value is only about 0.16. A longer  
252 coherent analysis time window tends to decrease the overall waveform coherency as more data  
253 including noise are put into the coherent analysis. However, a longer time window is beneficial  
254 for obtaining a stable migration result. The coherency of the coda wave is also included to benefit  
255 the source imaging. For this volcano earthquake dataset, tests show that the analysis time window  
256 needs to be at least 1 s to eliminate the influence of the noise and pure coda waves. We used a time  
257 window of 6 s for both events to make the migration results more stable.

258 Table 1 shows the quantitative location results of the different migration methods and the com-  
259 parison with the catalogue location. The origin time of this event for the MCM method in the table  
260 is estimated using the maximum coherent time plus the coherent analysis time window following  
261 Shi et al. (2018b). The event location of the MCM method shows the best correlation to the event  
262 location in the catalogue with less deviation in the location and origin time. Predicted P- and S-  
263 wave arrival times for this event in the catalogue and the event located by MCM are compared on  
264 record sections in Figure 6. The direct P- and S-wave arrivals correspond well with the predicted  
265 P- and S-wave arrival times for MCM location in most stations. Therefore the location determined  
266 by MCM of this event is acceptable.

267 Figure 3(b) shows the recorded three-component waveforms at station UTCA for the second  
268 event, whose local magnitude  $M_L$  is -0.29. The direct P-wave can be well identified in the vertical  
269 component and the direct S-wave can be well identified in the north-south and east-west com-  
270 ponents. The coda waves following the direct P- and S-waves are obvious. Figure 7 shows the  
271 vertical and horizontal profiles of the migration results for the four different waveform migration  
272 methods. As with the migration results of the previous event, the envelope and STA/LTA migra-  
273 tion methods do not focus the source energy appropriately. The migration results of the kurtosis  
274 and MCM method are quite similar. The horizontal locations of this event using the kurtosis and  
275 MCM method are consistent with the catalogue location with only little deviation. However, the  
276 located event depths of both kurtosis and MCM method are deeper than the event depth in the  
277 catalogue (1.72 km and 1.92 km deeper respectively). Nevertheless, compared to the horizontal  
278 location of the seismic event, the event depth is often not well constrained by the recorded data  
279 especially for surface arrays. The trade-off between event depth and origin time often makes event  
280 depth determination problematic and more difficult (Eisner et al. 2010). Figure 5(b) shows the  
281 stacking function of the MCM method at the position of the most coherent point. Table 2 shows  
282 the quantitative location results of the different migration methods and the comparisons with the  
283 catalogue. The location results of the MCM correspond very well with the catalogue in the hori-  
284 zontal directions (with very small deviations of 0.166 km and 0.181 km in the X and Y directions,  
285 respectively). Predicted P- and S-wave arrival times for this event in the catalogue and the event  
286 located by MCM are further compared on record sections in Figure 8. Probably because of the  
287 strong heterogeneity in the subsurface, the recorded waveforms at some stations are not very co-  
288 herent with the waveforms at other stations. However, the migration results of the MCM method  
289 are not seriously affected and seem still reliable. From the record sections of the vertical com-  
290 ponent (Figure 8 first row), we can clearly see the recorded direct P-wave arrivals show better  
291 consistency with the theoretical P-wave arrival times in the record section of the MCM method.  
292 This further demonstrates the reliability of the MCM location results.

293 The Uturuncu example shows that MCM can be used as a practical and precise seismic loca-  
294 tion method for automated volcano-tectonic and natural earthquake monitoring. As MCM utilizes

the waveform coherency across different stations, it performs better under high noise conditions and can obtain a more accurate location result compared to other migration-based location methods. Sparse monitoring arrays will decrease imaging resolution and cause location uncertainties. The utilization of multichannel coherency information in MCM can greatly expand available information used for location and improve imaging resolution (Shi et al. 2018b), which is critical for seismic event location using sparse monitoring arrays.

### 3.2 Locating triggered events on four hours of continuous waveform data

The  $M_w$  8.8 Maule earthquake on 27 February 2010 (at 06:34 UTC) triggered hundreds of earthquakes at Uturuncu with the passage of surface waves and the overtone phases of surface waves (Jay et al. 2012). Those triggered seismic swarms are recorded by the deployed Uturuncu monitoring arrays. According to Jay et al. (2012), the triggered events occurred with the onset of the Love and Rayleigh waves, and the earthquake rate reaches a maximum value of two events per minute with the passage of the Rayleigh wave overtones. We apply the MCM to automatically locate these triggered earthquakes using four hours of continuous data (06:00:00 to 10:00:00 UTC), which recorded most of the triggered events. The recorded waveform data at station UTCA are shown in Figure 9. As shown in the enlarged part of Figure 9, there are many small magnitude events which can be very difficult and time consuming to pick manually. As the triggered earthquakes start immediately after the surface wave train, many events occurred in a short time period with very close or overlapping waveform trains. Therefore, it will be very difficult to pick and associate different phases to a particular event. In addition, because of interference of noise and coda waves, it is also very difficult to accurately pick the P- and S-wave arrival times of small seismic events. The manual picking accuracy is highly dependent on human experience. The manual picking errors will inevitably cause location errors. As the MCM does not require picking and phase identification and the location accuracy of the MCM does not depend on event magnitude (waveform amplitude), it is very suitable to be used to automatically locate those dense triggered microseismic events.

The surface waves and surface wave overtones of the  $M_w$  8.8 Maule earthquake not only

322 trigger many seismic events in this area but also forms a big challenge for migration imaging  
323 using waveforms. Here, we filter waveforms using a frequency band of 4.2 - 21.6 Hz to exclude  
324 the influence of surface waves and low frequency noise. Because the sample rate (50 samples/s)  
325 is low, we suggest to use a long time window for coherency analysis in the MCM. Using a longer  
326 time window can improve the imaging stability and quality in noisy situations. We adopt a four  
327 second time window for both P- and S-waves in the MCM to resist the interference of noise  
328 and coda waves. Similarly, we only utilize the direct P-wave to conduct MCM for the vertical  
329 component data, and only utilize direct S-wave for the horizontal component data. The coherency  
330 value of the P-wave for the vertical component data and coherency values of the S-wave for the  
331 two horizontal component data are then stacked together to form the final migration value. For  
332 conventional waveform migration methods which stack amplitudes or characteristic functions of  
333 amplitudes, S-phases are often assigned higher weighting factors because S-phases tend to have  
334 higher amplitude. However, the S-phase often interferes with coda and converted waves, thus tends  
335 to have lower waveform coherency across different stations. In contrast, the P-phase which arrives  
336 first often has higher coherency despite its lower amplitude. Therefore, we assign a weighting  
337 factor of 0.6 to the P-phase of the vertical component and factors of 0.2 to the S-phases of each of  
338 the two horizontal components (east-west and north-south), noting that the MCM is insensitive to  
339 amplitudes.

340 The imaging area is 18 km, 15 km and 8 km in north-south, east-west and vertical directions,  
341 respectively (as shown in Figure 2 white rectangle area). The imaging point interval is 200 m in  
342 all different directions. Therefore, there are 283,556 imaging points in total. The time interval for  
343 searching for origin times is 0.08 s. The total number of searched origin times in the four hours is  
344 about 180,000. We assume that two earthquakes will not occur at the same time or within a few  
345 origin time samples (0.08 s). Therefore, at each searched origin time, we only save the imaging  
346 point which has the maximum coherency value. Figure 10 shows the variation of the maximum  
347 coherency value with different origin times in the four hours. When an earthquake occurs, at the  
348 correct origin time, the coherency values of each imaging point will all rise due to the arrival of  
349 the long waveform trains including direct, converted and coda waves. Therefore, we can observe

350 many local peaks rising from the background noise in Figure 10, which potentially correspond to  
351 seismic events. We use a coherency threshold of 0.1. By identifying the maximum value of each  
352 local peak, we can find the location and origin time of each seismic event. We identify 560 local  
353 peaks in Figure 10, which are viewed as potential seismic events. We then check each potential  
354 seismic event using the corresponding record sections of these potential seismic events and verify  
355 322 seismic events which have clear phase arrivals. The verified seismic events are shown as red  
356 dots in Figure 10. Although there are many events which do not show clear P- and S-phase arrivals,  
357 they may still be real seismic events, because the signal-to-noise ratio (SNR) for these events may  
358 be small (smaller than 1). Since the MCM has the ability to resist strong noise, it is not surprising  
359 that it can successfully identify seismic events below the noise level. The problem is that although  
360 identified by MCM, the weak seismic events with SNR below 1 cannot be effectively verified  
361 through their record sections at the present. By adopting stricter parameters (such as a higher  
362 coherency threshold, higher source prominence and longer origin time gap), we can also reduce  
363 the number of unverifiable seismic events and improve the proportion of confirmed seismic events.  
364 However, this would inevitably result in losing some small real seismic events which cannot be  
365 effectively verified by inspection of the record sections at the present. Therefore, further studies  
366 about detecting and verifying seismic events (especially events with low SNR) from migration  
367 traces/volumes are still needed. Here, since the verifying process is very quick and easy, in order  
368 to identify as many seismic events as possible, we adopt relatively relaxed parameters to identify  
369 the local maxima in the coherency time slice (Figure 10).

370 The existing catalogue has 114 seismic events in total in this four hour time period in this area,  
371 which are located by manual picking. For those 114 seismic events, 112 events (98.25%) have  
372 been successfully located by the MCM. In addition, the MCM has also automatically located 210  
373 more seismic events than the existing catalogue, which have been verified on the record sections.  
374 By checking the corresponding record sections, we find that the MCM not only automatically  
375 locates many more triggered seismic events than the catalogue, but also the origin time estimates  
376 of most events are more accurate than the existing catalogue under the current velocity models.  
377 This demonstrates that MCM is an efficient and reliable automatic location method. Figure 11

378 shows the locations of the 322 verified seismic events and the 114 current catalogue events. In the  
379 figure, we can see that the distribution of automatically located seismic events is consistent with  
380 that of the events in the catalogue. There are two main earthquake clusters. One is located in the  
381 northern part of the study area and close to the volcano. This earthquake cluster occurred earlier (6  
382 am to 8 am), and the events are mainly triggered by the surface waves (Love and Rayleigh waves)  
383 of the Maule earthquake. The other earthquake cluster occurred from 8 am to 10 am and is located  
384 in the southern part of the study area. The seismic events are mainly triggered by the surface wave  
385 overtones of the Maule earthquake.

386 Figure 12 shows a seismic event (referred to as event 1) which is both located by the MCM  
387 and the manual picking (catalogue). The MCM location result has a similar horizontal location  
388 as the catalogue result, but is deeper than the catalogue event. From the corresponding record  
389 sections (Figure 13), we can clearly see that the predicted arrival times of the MCM results have  
390 a much better correspondence with the P- and S-phase arrivals, especially for the S-phases of the  
391 horizontal components. This demonstrates that the MCM location results are reliable and have a  
392 better estimation of the origin times of seismic events. Figure 14 shows the migration profiles and  
393 record sections of a newly identified seismic event (referred to as event 2) by MCM, which is not  
394 in the existing catalogue. The source energy focuses nicely in the migration volume. The record  
395 sections which show clear P- and S-wave arrivals also indicate a real microseismic event occurred.  
396 It is worth noting that although event 2 is lower in event magnitude and has smaller amplitudes  
397 than event 1, the waveform coherency (0.22) of event 2 is higher than that of event 1 (0.17). For  
398 MCM, the waveform coherency not only depends on the amplitude (relating to event magnitude  
399 and SNR), but is also influenced by the interference of coda waves, converted waves and arrivals  
400 from other events. Thus, it is not surprising that a small seismic event can have higher waveform  
401 coherency and focussing of migration energy than a larger seismic event when the small event is  
402 less affected by interference of other non-coherent waves. This characteristic makes MCM very  
403 suitable for locating microseismic events.

404 Many more seismic events have been identified by MCM in this four hour time period than  
405 the published catalogue, which greatly complements the catalogue. We provide our extended cat-



406 alogue in the supplementary material. Figure 15 shows the number of triggered seismic events  
407 within the four hours. With this more complete catalogue, we find that rates of triggered events  
408 rise shortly after the passage of surface waves or surface wave overtones. Different to Jay et al.  
409 (2012), who conclude that rates of triggered events increased to a peak value of two events per  
410 minute with the passage of the X2/X3 Rayleigh wave overtones, we find that earthquake rates  
411 reach a peak value of about five events per minute after the passage the G1/R1 surface waves (Fig-  
412 ure 15). An increase of seismicity after the passage of X2/X3 is noticeable, but only reaches about  
413 three events per minute.

#### 414 **4 AQUISTORE SYNTHETIC DATA WITH REAL NOISE**

415 Synthetic waveform data with added Gaussian noise is often used in testing the performance of  
416 location algorithms. However in reality, the real noise field is not white, stationary or Gaussian  
417 (Birnie et al. 2016). Several noise studies have shown that seismic noise is often variable in space  
418 and time, leading to increased difficulty in source imaging (Birnie et al. 2017). In this section,  
419 we apply the MCM location algorithm to the Aquistore noise dataset to examine the location  
420 performance in the presence of real seismic noise. The Aquistore noise data have been extracted  
421 from a permanent surface array installed at the Aquistore carbon dioxide storage site (Roach et al.  
422 2015; Birnie et al. 2016, 2017). The monitoring data used here were recorded by the surface  
423 array during the drilling and construction phase of the injection and observation wells prior to  
424 CO<sub>2</sub> injection. Therefore, significant drilling noise and non-stationary noise were recorded in the  
425 dataset. No injection-related or induced seismic events are recorded in this period, which makes  
426 the recorded time-series an excellent dataset for investigating the effect of real seismic noise on  
427 seismic location. Figures 16 (a) and (b) show the surface array geometry and velocity model of  
428 the Aquistore area. The surface array consists of 50 buried geophones (34 in North-south direction  
429 and 16 in East-west direction) with a sampling frequency of 500 Hz.

430 We generate waveform seismic data using the propagator matrix technique of Zhu & Rivera  
431 (2002) for both a shallow and a deep event (Figures 16 (c-e)). The shallow and deep events are  
432 located at a depth of 2.55 km and 3.15 km, respectively. The deep event has been placed in a thin

433 and relatively low velocity layer. There are also many thin layers above and below the deep event  
434 (Figures 16 (b-e)), which may cause difficulty in imaging the deep event. We use the shallow and  
435 deep events to examine the influence of complex velocity model on the migration result. For both  
436 the shallow and deep event, a  $45^\circ$  dip-slip double-couple source with 40 Hz peak frequency is used  
437 to give a specified radiation pattern. The recorded real noise (Birnie et al. 2016) is added to the  
438 synthetic data to mimic as closely as possible a ‘real’ dataset with varying signal-to-noise ratios.  
439 The SNR is defined by the ratio of the maximum amplitude between signal and noise. This kind  
440 of semi-synthetic dataset enables a quantitative evaluation of the location errors in the presence of  
441 different realistic noise scenarios and has been employed to evaluate the monitoring performance  
442 of a dedicated seismic monitoring array (López-Comino et al. 2017). The synthetic data and noise  
443 data are shown in Figure 17. After adding noise, the arrival of the direct P-wave cannot be easily  
444 recognized. Stations 18-24 and 41-43 are deployed near the injection and observation well (as  
445 shown in Figure 16(a)), and thus are seriously contaminated by drilling noise (Figure 17c). The  
446 non-stationarity and spatial variability of the noise will make event location more difficult.

#### 447 **4.1 Location results for shallow event**

448 We compare the location results of different migration methods using waveform envelope, STA/LTA  
449 and kurtosis as characteristic functions and also the MCM method for different SNRs. The same  
450 monitored real noise of different levels have been added into the synthetic dataset to make the  
451 semi-synthetic datasets of different SNRs. The SNRs are chosen to be infinite (noise free), 1, 0.5,  
452 0.25 and 0.025 respectively. We then analyse the influence of SNRs to location results and com-  
453 pare the performance of different migration methods under different SNR situations. Figure 18  
454 compares the migration results for the four different methods when the SNR is 1 (for a complete  
455 comparison of different SNRs, see supplementary material Figures S.1-S.3). When the SNR is  
456 larger than 0.25, the MCM exhibits the best resolution and location performance in both the hor-  
457 izontal and vertical directions. Due to the use of the derivative (Langet et al. 2014), the kurtosis  
458 seems to have better resolution in the XZ profile (as shown in Figure 18). However the location  
459 results of kurtosis migration are often biased due to the trade-off between depth and origin time.

460 The results also show that receiver distribution influences the results of the locations. Compared  
 461 to the X direction, the image in the Y direction relies on fewer geophones leading to increased  
 462 location uncertainty in that direction, and therefore the envelope, STA/LTA and kurtosis methods  
 463 show poorer resolution in the Y direction (as shown in Figure 18). However the MCM still main-  
 464 tains very good resolution in the Y direction. The location results of the envelope, STA/LTA and  
 465 kurtosis methods are often biased in the Z direction. When the SNR is below 0.25, the MCM fails  
 466 to locate the source, because the noise recorded during drilling and construction of the injection  
 467 well is pervasive over all the traces, especially notable in the traces which are close to the injection  
 468 well. The drilling and construction noise coming from the injection well is continuous in time, and  
 469 so leads to continuous coherent noise on all the traces. When the SNR is below 0.25, the drilling  
 470 noise dominates the wavefield in all the traces. The continuous (both in space and time) and co-  
 471 herent drilling noise contributes to the failure of the MCM method when the SNR is below 0.25.  
 472 The other methods also fail to locate the source accurately because of strong noise contamination.  
 473 When the SNR is 0.025, all the methods fail to locate the source. However, approaches have been  
 474 developed to 'whiten' the noise and hence to reduce the influence of coherent noise (Birnie et al.  
 475 2017).

476 The automatic weighting scheme can be integrated into the multidimensional MCM flexibly  
 477 (Shi et al. 2018b), which gives MCM the ability to conduct automatic quality control of the input  
 478 data. We devise an automatic quality control scheme to deal with the drilling noise and surmount  
 479 the SNR limit in the presence of continuous drilling noise. The automatic quality control scheme  
 480 comprises weighting and filtering. The weighting factors (Shi et al. 2018b, equation 3) are deter-  
 481 mined by evaluating the amplitude of each trace. Because the continuous drilling noise will nor-  
 482 mally contaminate a whole trace, here we use an average absolute amplitude ratio to discriminate  
 483 very noisy traces and apply a weighting coherency calculation scheme to all traces. The absolute  
 484 amplitude ratio of a trace is defined as the ratio of the average absolute amplitude of the trace to the  
 485 average absolute amplitude of all traces ( $a_i = \overline{|\mathbf{d}_i|} / \overline{|\mathbf{D}|}$ ,  $a_i$  is the absolute amplitude ratio of the  $i$ -th  
 486 trace,  $\mathbf{d}_i$  is the waveform amplitudes of the  $i$ -th trace and  $\mathbf{D}$  is the amplitudes of all traces). Figure  
 487 19 shows the absolute amplitude ratios of different stations for the noisy datasets with different

488 SNRs. For traces which are highly contaminated by continuous drilling noise, the energy of this  
489 trace will be much larger than the average energy over the whole traces, which will contribute to a  
490 high absolute amplitude ratio (as shown in Figure 19). Through inspecting the absolute amplitude  
491 ratios of all traces, we can identify high quality traces and thus stabilize the migration result. We  
492 set an absolute amplitude ratio limit of 1.5. Above this limit, the weighting factor of this trace will  
493 be set to 0, otherwise the weighting factors are 1. Because our waveform coherency is evaluated  
494 through correlation coefficient, the absolute value of the amplitude will not affect the coherency  
495 calculation. Therefore, weighting values of 0 or 1 rather than sliding values are assigned to exclude  
496 or include traces in the coherency calculation. Through weighting, we select high quality data to  
497 conduct migration and exclude traces with very high absolute amplitude ratio (which means ex-  
498 tremely low SNR for that trace). As shown in Figure 19, traces 19-24 and 41-43 which are close to  
499 the observation and injection wells are highly contaminated by the drilling noise (consistent with  
500 Figures 16 and 17). Therefore, after weighting these traces will be excluded from the dataset used  
501 for imaging. Before calculating multichannel waveform coherency or characteristic functions, the  
502 selected data are filtered in the frequency domain. Because the drilling and construction of the in-  
503 jection well are low-frequency processes, we applied a 6th-order highpass Butterworth filter with  
504 a cutoff frequency of 50 Hz to the semi-synthetic data to remove the low frequency drilling noise.

505 The migration results with automatic quality control scheme (weighting and filtering) are  
506 shown in Figure 20 and the SNR before filtering is 0.025 (for a complete comparison of dif-  
507 ferent SNRs, see supplementary materials Figures S.4-S.6). Through the automatic quality control  
508 scheme, the imaging quality of the four migration methods becomes better and the imaging reso-  
509 lution also improves especially for low SNR scenarios. The MCM exhibits better location results  
510 with higher resolution compared to the other methods for all SNR situations. When the SNR is  
511 above 0.025, MCM can locate the source accurately without deviation, while the other three meth-  
512 ods all have location deviations. When the SNR is 0.025, only the MCM can locate the source  
513 correctly with a minimal deviation of 20 m. With such a low SNR, the STA/LTA method focused  
514 at the shallow part of the true source position with very low imaging resolution, while the kur-  
515 tosis method cannot focus correctly. Because of the non-Gaussian property of the real noise and

516 the sensitivity of the characteristic function of the kurtosis method, the kurtosis method is more  
517 susceptible to the array geometry. An irregular and/or sparse monitoring array will tend to bias the  
518 location results of the kurtosis method. Thus the location results of the kurtosis method are less sta-  
519 ble compared to the other three methods. Figure 21 shows the location errors of the four methods  
520 under different SNRs with/without automatic quality control scheme. The MCM method outper-  
521 forms the other methods at all noise levels when the automatic quality control scheme is applied  
522 (Figure 21(b)). The implemented automatic quality control scheme using filtering and weighting  
523 can effectively improve the location accuracy for most tested methods.

## 524 **4.2 Location results for deep event**

525 The location results for the deep event with a SNR of 1 are shown in Figure 22. Since the SNR  
526 is relatively high, for consistency and better comparison with the migration results of the shallow  
527 event (Figure 18), original data without automatic quality control are used for migration. The  
528 velocity model above the deep event is more complicated as it contains thin layers and large  
529 velocity contrasts. However, compared to the shallow event, the location results of the deep event  
530 are not seriously affected by the complexity of the velocity model. Due to the increase of the  
531 velocity in the imaging area, the arrival time differences between the adjacent imaging points  
532 become smaller, which is detrimental for distinguishing the phase arrivals. Correspondingly the  
533 imaging resolution for all the 4 methods decreases compared to imaging results of the shallow  
534 event (as can be seen in the comparison of Figure 18 and 22). The imaging results of the envelope  
535 and STA/LTA methods still have large deviations in the vertical direction, while the MCM and  
536 kurtosis methods locate the deep event accurately. The imaging results of the MCM exhibit high  
537 resolution in the horizontal direction. However, the resolution in the vertical direction deteriorates  
538 compared to the results of the shallow event. The degradation of the vertical resolution is related  
539 to the chosen length of the time window of the coherence analysis as well as the velocity of  
540 the imaging area. Although the same time window is applied in the imaging of the shallow and  
541 deep events, the higher velocity of the deep event layer contributes to the reduction of the vertical

542 resolution. Using a smaller time window can improve the imaging resolution, but at the expense  
543 of reducing noise suppression ability.

544 Figure 23 shows the stacking functions of the four methods at the true source location of the  
545 deep event. The four methods all exhibit excellent source prominence at the correct origin time.  
546 Time windows for both P- and S-phases are simultaneously used in the migration. The pink area  
547 around  $-0.6$  second in Figure 23 highlights the time range where P-phases move into the stacking  
548 window of the S-phases when searching for origin time. Meanwhile, the pink area around  $0.7$   
549 second highlights the time range where S-phases move into the stacking window of the P-phases.  
550 For the stacking functions of the envelope and STA/LTA methods, a notable peak can be observed  
551 at these times. However, the MCM can effectively suppress this kind of disturbance and avoid  
552 identifying unrealistic events.

553 From the results of the Aquistore dataset, we can see that MCM can be used as an effective  
554 migration method to automatically locate microseismic events induced by fluid injection or hy-  
555 draulic fracturing. Although drilling or injection noise can pose big challenges for source imaging,  
556 different ways can be adopted to acquire reliable seismic location results. Irregularly distributed  
557 monitoring arrays will lead to unbalanced imaging resolution in different directions. However, due  
558 to the utilization of multichannel waveform coherency, MCM can acquire higher and much more  
559 balanced imaging resolution in different directions compared to other migration-based methods.  
560 As traveltimes differences between adjacent imaging points in low velocity zone are larger, the  
561 imaging results in the low velocity zone (i.e. a shallow event) are better than those in a high veloc-  
562 ity zone (i.e. at greater depths), and the source imaging resolution in the low velocity zone is also  
563 higher than that in the high velocity zone.

## 564 **5 DISCUSSION**

565 For the synthetic data case, the stacked coherency trace will normally exhibit a flat top as we have  
566 discussed in detail in Shi et al. (2018b). However, for real data, such flat tops may not exist because  
567 of strong interference from noise and coda waves (as shown in Figure 5). Typically, one records  
568 and takes the time and position which has the maximum coherency value as the origin time and

569 location of a seismic event. However due to a systematic bias between the origin time and the  
570 maximum coherent time, calibration is needed in order to obtain an accurate estimation of the  
571 origin time of the seismic event. As shown in Figure 24, similar to synthetic data, the coherency  
572 will start to rise at one coherent analysis time window (referred to as  $T_w$ ) before the correct source  
573 origin time (referred to as  $T_0$ ). For real seismic data, because of subsurface heterogeneity, there  
574 are many coda waves following the direct P- and S-phases. Those coda waves often show lower  
575 coherency compared to direct phases and have high amplitudes compared to background noise.  
576 Here, we assume the coda waves are incoherent. Therefore, the maximum coherency value will  
577 appear one period (referred to as  $T$ ) of the direct phase after the rise of the coherency. That is to say  
578 the maximally coherent time (referred to as  $T_{max}$ ) is  $T_w - T$  ahead of the correct source origin  
579 time. So the calibration equation for source origin time is  $T_0 = T_{max} + T_w - T$ . Since it is easy to  
580 obtain a good estimate of the period of the direct phase, we can perform the origin time calibration  
581 easily and efficiently. If the direct phases have high SNR and coda waves are partly coherent,  
582 we may see a small flat top around  $T_{max}$  or the maximum coherency value appears around the  
583 theoretical maximally coherent time (as shown in Figure 24 the dashed line). Thus in this situation,  
584 the estimate of the origin time will be affected and shows a small deviation. However, according to  
585 our experience of processing the Uturuncu dataset, after calibration we can have a good estimation  
586 of source origin times. Finally, in the stacked coherency trace, waveform coherency will decrease  
587 to background noise level at one coherent analysis time window after the maximally coherent time.

588 For the Uturuncu dataset, only a few stations are available for source location, which negatively  
589 affects the MCM imaging. However compared to other migration-based methods, in spite of the  
590 very sparse monitoring array, MCM still obtains more reliable and precise location results by the  
591 use of multichannel waveform coherency. A dense array with wide aperture and azimuth coverage  
592 will greatly improve the imaging quality, especially when a long analysis time window is used.  
593 When the stations are widely spread, the traveltimes differences to different stations will be large.  
594 Thus the migration result of the MCM will be better and the influence of the continuous coda  
595 waves can also be reduced. High frequency information in the recorded data is important for  
596 improving the imaging resolution. For the Uturuncu dataset, because of a low sampling rate, the

597 highest effective frequency is limited to 25 Hz. The volcano-tectonic earthquakes often contain  
598 high-frequency content above this cut-off frequency. The insufficient sampling of the waveform  
599 data (as can be seen in the Figure 3(b)) has limited the imaging resolution and quality. Despite the  
600 sparse recording array and the lack of high frequency content, the MCM still obtains reliable event  
601 locations. When possible, we recommend volcano monitoring arrays record at at least 100 Hz to  
602 facilitate future automatic volcano-tectonic event determination.

603 For natural earthquakes, strong coda waves are often observed in the seismograms. The strong  
604 coda waves can have a significant influence on the envelope of the waveforms and can also seri-  
605 ously affect the event detection using approaches such as STA/LTA and kurtosis. Thus the location  
606 performance of the envelope, STA/LTA and kurtosis migration methods will be negatively affected  
607 by the coda waves. Only when the coda waves of different stations are long-lasting and coherent,  
608 they will have a negative impact on the MCM migration. The continuous coherent coda waves  
609 will make the MCM source imaging ambiguous. One way to deal with coherent coda waves is to  
610 increase the analysis time window for the coherency calculation. By using a longer time window,  
611 the whole waveform train can be included in the coherent analysis and the direct P- or S-waves  
612 as well as the coda waves are utilized to image the source event. Thus in this way the coherency  
613 of the coda waves can be fully utilized to improve the event location, however at the expense of  
614 reducing the imaging resolution. If coda waves are incoherent, a short analysis time window is  
615 suggested to improve waveform coherency value and imaging resolution.

616 For event location at the Uturuncu, although the same velocity model used in obtaining the  
617 event catalogue is utilized for location here, the event locations of the waveform migration method  
618 are different to the event location in the catalogue, especially in event depth. The discrepancy  
619 may come from different types of information being used in the event location. For events in the  
620 catalogue, only the arrival times of the direct P- and S-waves obtained by manual picking are  
621 used in the event location. However for waveform migration methods, the recorded waveforms  
622 from different stations are directly used to locate the seismic event. MCM automatically identify  
623 the maximum coherent time according to recorded traces and the predicted phase arrival times  
624 are thus slightly different from the manually picked arrival times. Regardless of velocity model,



625 the location result of the arrival time based methods will be affected by the accuracy of manual  
626 picking, especially for low magnitude events. The location result of migration based methods  
627 is mainly affected by the signal-to-noise ratio and medium heterogeneity, which influence the  
628 recorded waveforms.

629 In the record sections (Figures 6 and 8), the recorded direct P- and S-wave arrivals at some  
630 stations do not show a good consistency with the theoretical arrival times. And despite most direct  
631 P-wave arrivals corresponding very well to the theoretical arrival times, the recorded S-waves  
632 often arrive earlier than the theoretical S-wave arrival times. This discrepancy likely comes from  
633 the velocity model used in the event location. Here we just applied a layered velocity model with a  
634 constant  $v_p/v_s$  ratio of 1.75. In reality, the subsurface can have strong lateral velocity heterogeneity  
635 as well as varying  $v_p/v_s$  ratio. The S-wave velocity model obtained by ambient noise tomography  
636 (Jay et al. 2012) reveals the velocity heterogeneity in the Uturuncu area. If the velocity model is  
637 very rough, it is worthwhile to adopt a method which can simultaneously locate the source and  
638 update the velocity model. In this way, we can improve the event location accuracy and obtain a  
639 more precise velocity model at the same time. By adjusting both the event location and velocity  
640 model iteratively, the location results can match the arrivals of seismic phases more precisely.  
641 Nevertheless, this is beyond the scope of this study.

642 For general waveform location methods based on the stacking of characteristic functions, the  
643 imaging resolution in different directions is highly dependent on the array distribution. More geo-  
644 phones in a certain spatial direction increases resolution in that direction. However, if one direction  
645 is better sampled than the other directions, the imaging results will be dominated by the waveform  
646 stacking in that direction. Thus the imaging resolution in other directions (especially in the per-  
647 pendicular direction) will be degraded (as can be seen in the comparison between the first and  
648 second rows in Figure 18). If we want to achieve equal resolution in different directions when  
649 locating the source, evenly distributed geophones are required. However, MCM utilizes the co-  
650 herency between all possible receiver pairs, therefore the information from different directions  
651 can achieve a better balance improving the MCM locations compared to the other methods. For  
652 an irregularly distributed monitoring array, assuming  $n_p$  stations have been deployed in the pre-

653 dominant direction, whereas  $n_c$  stations ( $n_p > n_c$ ) are deployed in the non-predominant direc-  
 654 tion. The contribution from non-predominant direction to the whole migrated volume for MCM  
 655 ( $2n_p n_c / [(n_p + n_c)(n_p + n_c - 1)]$ ) is always higher than that for conventional migration-based  
 656 methods ( $n_c / (n_p + n_c)$ ). For MCM, due to the use of multichannel waveform coherency across  
 657 all the stations, the effective information from non-predominant direction can occupy a higher  
 658 proportion in migration compared to other conventional single-channel-based location methods.  
 659 Therefore, the imaging results of MCM are less affected by the irregular distribution of the re-  
 660 ceivers, and the imaging resolution in different directions are well balanced.

661 As shown in the imaging results of the Aquistore real noise data, the location results of the  
 662 envelope and STA/LTA methods often show large deviations in depth. This is because the charac-  
 663 teristic functions such as envelope and STA/LTA cannot represent the arrival times of the P- and  
 664 S-phases accurately. For envelope and STA/LTA, the maximum value of the characteristic func-  
 665 tion often appears later than the correct arrival times of the P- and/or S-waves. For example, if the  
 666 source time function is a Ricker wavelet, the maximum value of the envelope is located at the peak  
 667 amplitude of the P- and S-phases, not at the accurate arrival times of the P- and S-phases, i.e. a half-  
 668 period later. The characteristic function represents a transformation on the original waveform, and  
 669 the transformation on recorded waveforms of different stations can have different effects because  
 670 of noise, source radiation pattern, instrument response, etc. Thus the delayed times corresponding  
 671 to the correct arrival times can be different for different traces. This will lead to a trade-off between  
 672 the location depth and the origin time of the event. Finally, both the depth and origin time of the  
 673 location results can be biased. For the kurtosis method, due to the application of the derivative  
 674 of kurtosis (Langet et al. 2014), it can represent the arrival times of the P- and S-waves more ac-  
 675 curately. Thus less deviations in depth are observed in the location results. However, the kurtosis  
 676 method is more affected by noise and irregular array geometry. The location results are not stable  
 677 compared to the other methods, and deviations in depth can easily appear when it cannot represent  
 678 the arrival time correctly. For MCM, due to the use of multichannel waveform coherency among  
 679 different traces, the maximum coherency value will appear at the correct arrival times of the P-  
 680 and S-waves and waveform coherency will decrease rapidly when they deviate from the correct

681 source location (Shi et al. 2018b). There is less trade-off between location depth and origin time.  
682 Therefore, the MCM can accurately identify the source location and also the origin times with  
683 higher resolution.

684 Continuous coherent noise such as drilling noise remains a challenge for MCM. The coherent  
685 noise which is continuous both in space and time will lead to high coherency values between  
686 all receiver pairs, thus contributing to the failure of MCM when the coherent noise level is too  
687 high. Removing the continuous coherent noise is key to overcoming this problem. If the coherent  
688 noise in the recorded data falls into a specific frequency band, we can use frequency filtering or  
689 frequency-wavenumber filtering to remove the coherent noise and improve the imaging quality.  
690 For microseismic monitoring, the main coherent noise such as the drilling noise and injection  
691 noise are often low frequency noise (less than tens of Hz), while the dominant frequency of the  
692 microseismic signals are often relatively very high (from tens to thousands of Hz). Therefore,  
693 this kind of low frequency noise can be separated and removed from the microseismic dataset by  
694 filtering. Automatic quality control techniques such as weighting and filtering are effective ways  
695 to mitigate the effects of noise and improve imaging quality.

## 696 **6 CONCLUSIONS**

697 In this paper, we applied the MCM method (Shi et al. 2018b) to locate microseismic events in  
698 a reservoir and a volcanic setting in the presence of realistic noise. The location results of trig-  
699 gered volcano-tectonic earthquakes demonstrate the feasibility of using MCM method to locate  
700 natural earthquakes recorded by sparse arrays. The MCM can automatically locate many triggered  
701 events which are difficult and time consuming to manually pick. The MCM has the ability to lo-  
702 cate microseismic events which are otherwise often neglected by researchers. Using MCM, we can  
703 efficiently obtain a more complete catalogue, which can help us better understand the subsurface  
704 earthquake process. The newly obtained seismic catalogue at Uturuncu using MCM can be found  
705 in the supplementary material. The predicted arrival times of P- and S-phases at different stations  
706 are also attached, which can be used for further studies such as relocation. Compared to other  
707 migration based methods, MCM shows more reliable location results and performs better in high

708 noise, sparse monitoring array and strong coda situations. The Aquistore real noise case demon-  
709 strates the excellent imaging performance of the MCM in the presence of strong realistic noise.  
710 Even though strong coherent noise exists in all traces, the MCM can still locate the source accu-  
711 rately. Usual quality control techniques such as the frequency filtering and weighting are feasible  
712 ways to remove coherent drilling or injection noise, the latter of which we employ in an automatic  
713 way. Compared to the other methods, the location results of the MCM have higher resolution and  
714 are more stable.

715 Computational efficiency tests of the MCM show that the MCM is highly scalable and par-  
716 allelizable. The parallel MCM code can achieve a high speedup ratio easily, which gives MCM  
717 the ability to perform real time processing. Seismic location with sparse and/or irregularly dis-  
718 tributed monitoring array is problematic and difficult. MCM can expand the effective informa-  
719 tion used for locating by calculating multichannel waveform coherency across different stations,  
720 thus in this way improving the location performance with sparse array. When the monitoring ar-  
721 ray is irregularly distributed, MCM imaging resolution in different directions can also be well  
722 balanced due to the use of pairwise handling among all available stations. Compared to other  
723 single-channel-based location methods, the location result of MCM is less affected by the irreg-  
724 ular and/or sparse distribution of the receivers, and the imaging resolutions in different direc-  
725 tions are higher and well balanced. The MCM code is open source and can be downloaded from  
726 <https://github.com/speedshi/seisloc>. The MCM code is written in FORTRAN and further  
727 developments of the MCM software will be released in the future.

## 728 **7 ACKNOWLEDGEMENTS**

729 We would like to thank Claire Birnie and the Petroleum Technology Research Centre (PTRC) for  
730 access to Aquistore Data. Aquistore is an independent research and monitoring project managed by  
731 the PTRC which intends to demonstrate that storing liquid carbon dioxide (CO<sub>2</sub>) deep underground  
732 (in a brine and sandstone water formation), is a safe, workable solution to reduce greenhouse gases  
733 (GHGs). Seismic data for the Uturuncu volcano-tectonic earthquakes were obtained via the IRIS  
734 DMC from stations in 'The life cycle of Andean volcanoes:Combining space-based and field stud-

735 ies (ANDIVOLC/Cornell)' Network run by the Cornell University (doi: 10.7914/SN/YS\_2009).  
 736 A. Nowacki is supported by a Leverhulme Early Career Fellowship and the Natural Environment  
 737 Research Council (grant NE/R001154/1).

## 738 REFERENCES

- 739 Bai, C.-y. & Kennett, B., 2000. Automatic phase-detection and identification by full use of a single three-  
 740 component broadband seismogram, *Bull. Seismol. Soc. Am.*, **90**(1), 187–198.
- 741 Barkved, O., Gaucher, E., Hornby, B., Kristiansen, T., & Maisons, C., 2002. Analysis of seismic recordings  
 742 during injection using in-well permanent sensors, in *64th EAGE Conference & Exhibition*.
- 743 Birnie, C., Chambers, K., Angus, D., & Stork, A. L., 2016. Analysis and models of pre-injection surface  
 744 seismic array noise recorded at the Aquistore carbon storage site, *Geophys. J. Int.*, **206**(2), 1246–1260.
- 745 Birnie, C., Chambers, K., & Angus, D., 2017. Seismic arrival enhancement through the use of noise  
 746 whitening, *Phys. Earth Planet. In.*, **262**, 80–89.
- 747 Cesca, S. & Grigoli, F., 2015. Chapter two-full waveform seismological advances for microseismic mon-  
 748 itoring, *Adv. Geophys.*, **56**, 169–228.
- 749 Drew, J., White, R. S., Tilmann, F., & Tarasewicz, J., 2013. Coalescence microseismic mapping, *Geophys.*  
 750 *J. Int.*, **195**(3), 1773–1785.
- 751 Eisner, L., Hulse, B., Duncan, P., Jurick, D., Werner, H., & Keller, W., 2010. Comparison of surface and  
 752 borehole locations of induced seismicity, *Geophys. Prospect.*, **58**(5), 809–820.
- 753 Gharti, H. N., Oye, V., Roth, M., & Kühn, D., 2010. Automated microearthquake location using envelope  
 754 stacking and robust global optimization, *Geophysics*, **75**(4), MA27–MA46.
- 755 Gibowicz, S. J. & Kijko, A., 2013. *An introduction to mining seismology*, vol. 55, Elsevier.
- 756 Grigoli, F., Cesca, S., Amoroso, O., Emolo, A., Zollo, A., & Dahm, T., 2013a. Automated seismic event  
 757 location by waveform coherence analysis, *Geophys. J. Int.*, **196**(3), 1742–1753.
- 758 Grigoli, F., Cesca, S., Vassallo, M., & Dahm, T., 2013b. Automated seismic event location by travel-time  
 759 stacking: An application to mining induced seismicity, *Seismol. Res. Lett.*, **84**(4), 666–677.
- 760 Grigoli, F., Cesca, S., Krieger, L., Kriegerowski, M., Gammaldi, S., Horalek, J., Priolo, E., & Dahm, T.,  
 761 2016. Automated microseismic event location using master-event waveform stacking, *Sci. Rep.*, **6**, 25744.
- 762 Jay, J. A., Pritchard, M. E., West, M. E., Christensen, D., Haney, M., Minaya, E., Sunagua, M., McNutt,  
 763 S. R., & Zabala, M., 2012. Shallow seismicity, triggered seismicity, and ambient noise tomography at  
 764 the long-dormant Uturuncu Volcano, Bolivia, *Bull. Volcanol.*, **74**(4), 817–837.
- 765 Kao, H. & Shan, S.-J., 2007. Rapid identification of earthquake rupture plane using Source-Scanning  
 766 Algorithm, *Geophys. J. Int.*, **168**(3), 1011–1020.
- 767 Knudsen, S., Havsgård, G., Berg, A., & Bostick, T., 2006. Flow-induced noise in fiber-optic 3C seismic

- 768 sensors for permanent tubing-conveyed installations, in *68th EAGE Conference and Exhibition incorporating SPE EUROPEC 2006*.
- 769
- 770 Langet, N., Maggi, A., Michelini, A., & Brenguier, F., 2014. Continuous Kurtosis-based migration for  
771 seismic event detection and location, with application to Piton de la Fournaise Volcano, La Réunion,  
772 *Bull. Seismol. Soc. Am.*, **104**(1), 229–246.
- 773 Lavallée, Y., Meredith, P., Dingwell, D., Hess, K., Wassermann, J., Cordonnier, B., Gerik, A., & Kruhl, J.,  
774 2008. Seismogenic lavas and explosive eruption forecasting, *Nature*, **453**(7194), 507.
- 775 López-Comino, J., Cesca, S., Kriegerowski, M., Heimann, S., Dahm, T., Mirek, J., & Lasocki, S., 2017.  
776 Monitoring performance using synthetic data for induced microseismicity by hydrofracking at the Wysin  
777 site (Poland), *Geophys. J. Int.*, **210**(1), 42–55.
- 778 Maggi, A., Tape, C., Chen, M., Chao, D., & Tromp, J., 2009. An automated time-window selection  
779 algorithm for seismic tomography, *Geophys. J. Int.*, **178**(1), 257–281.
- 780 McNutt, S. R., 1996. Seismic monitoring and eruption forecasting of volcanoes: a review of the state-of-  
781 the-art and case histories, in *Monitoring and mitigation of volcano hazards*, pp. 99–146, Springer.
- 782 Peng, Z. & Zhao, P., 2009. Migration of early aftershocks following the 2004 Parkfield earthquake, *Nat.*  
783 *Geosci.*, **2**(12), 877.
- 784 Power, D. V., Schuster, C. L., Hay, R., Twombly, J., et al., 1976. Detection of hydraulic fracture orientation  
785 and dimensions in cased wells, *J. Pet. Technol.*, **28**(09), 1–116.
- 786 Pritchard, M., 2009. The life cycle of Andean volcanoes: Combining space-based and field studies, *Inter-*  
787 *national Federation of Digital Seismograph Networks. Other/Seismic Network. 10.7914/SN/YS\_2009*.
- 788 Pritchard, M. & Simons, M., 2004. An InSAR-based survey of volcanic deformation in the central Andes,  
789 *Geochem. Geophys. Geosyst.*, **5**(2).
- 790 Roach, L. A., White, D. J., & Roberts, B., 2015. Assessment of 4D seismic repeatability and CO<sub>2</sub> detection  
791 limits using a sparse permanent land array at the Aquistore CO<sub>2</sub> storage site, *Geophysics*, **80**(2), WA1–  
792 WA13.
- 793 Shi, P., Angus, D., Nowacki, A., Yuan, S., & Wang, Y., 2018a. Microseismic Full Waveform Modeling in  
794 Anisotropic Media with Moment Tensor Implementation, *Surv. Geophys.*, **39**(4), 567–611.
- 795 Shi, P., Angus, D., Rost, S., Nowacki, A., & Yuan, S., 2018b. Automated seismic waveform location using  
796 Multichannel Coherency Migration (MCM)—I. Theory, *Geophys. J. Int.*.
- 797 Shi, P., Yuan, S., Wang, T., Wang, Y., & Liu, T., 2018c. Fracture Identification in a Tight Sandstone Reser-  
798 voir: A Seismic Anisotropy and Automatic Multisensitive Attribute Fusion Framework, *IEEE Geosci.*  
799 *Remote Sens. Lett.*, **15**(10), 1525–1529.
- 800 Sparks, R. S. J., Folkes, C. B., Humphreys, M. C., Barfod, D. N., Clavero, J., Sunagua, M. C., McNutt,  
801 S. R., & Pritchard, M. E., 2008. Uturuncu volcano, Bolivia: Volcanic unrest due to mid-crustal magma  
802 intrusion, *Am. J. Sci.*, **308**(6), 727–769.

- 803 Verdon, J., Kendall, J.-M., White, D., & Angus, D., 2011. Linking microseismic event observations with  
804 geomechanical models to minimise the risks of storing CO<sub>2</sub> in geological formations, *Earth Planet. Sci.*  
805 *Lett.*, **305**(1), 143–152.
- 806 Verdon, J. P., Kendall, J.-M., White, D. J., Angus, D. A., Fisher, Q. J., & Urbancic, T., 2010. Passive  
807 seismic monitoring of carbon dioxide storage at Weyburn, *The Leading Edge*.
- 808 Wilks, M., Kendall, J.-M., Nowacki, A., Biggs, J., Wookey, J., Birhanu, Y., Ayele, A., & Bedada, T., 2017.  
809 Seismicity associated with magmatism, faulting and hydrothermal circulation at Aluto Volcano, Main  
810 Ethiopian Rift, *J. Volcanol. Geoth. Res.*.
- 811 Xu, N., Tang, C., Li, L., Zhou, Z., Sha, C., Liang, Z., & Yang, J., 2011. Microseismic monitoring and  
812 stability analysis of the left bank slope in Jinping first stage hydropower station in southwestern China,  
813 *Int. J. Rock Mech. Min. Sci.*, **48**(6), 950–963.
- 814 Yuan, S., Wang, S., Ma, M., Ji, Y., & Deng, L., 2017. Sparse Bayesian learning-based time-variant decon-  
815 volution, *IEEE Trans. Geosci. Remote Sens.*, **55**(11), 6182–6194.
- 816 Yuan, S., Liu, J., Wang, S., Wang, T., & Shi, P., 2018a. Seismic waveform classification and first-break  
817 picking using convolution neural networks, *IEEE Geosci. Remote Sens. Lett.*, **15**(2), 272–276.
- 818 Yuan, S., Wang, S., Luo, C., & Wang, T., 2018b. Inversion-Based 3-D Seismic Denoising for Exploring  
819 Spatial Edges and Spatio-Temporal Signal Redundancy, *IEEE Geosci. Remote Sens. Lett.*, (99), 1–5.
- 820 Zhebel, O. & Eisner, L., 2014. Simultaneous microseismic event localization and source mechanism  
821 determination, *Geophysics*, **80**(1), KS1–KS9.
- 822 Zhu, L. & Rivera, L. A., 2002. A note on the dynamic and static displacements from a point source in  
823 multilayered media, *Geophys. J. Int.*, **148**(3), 619–627.

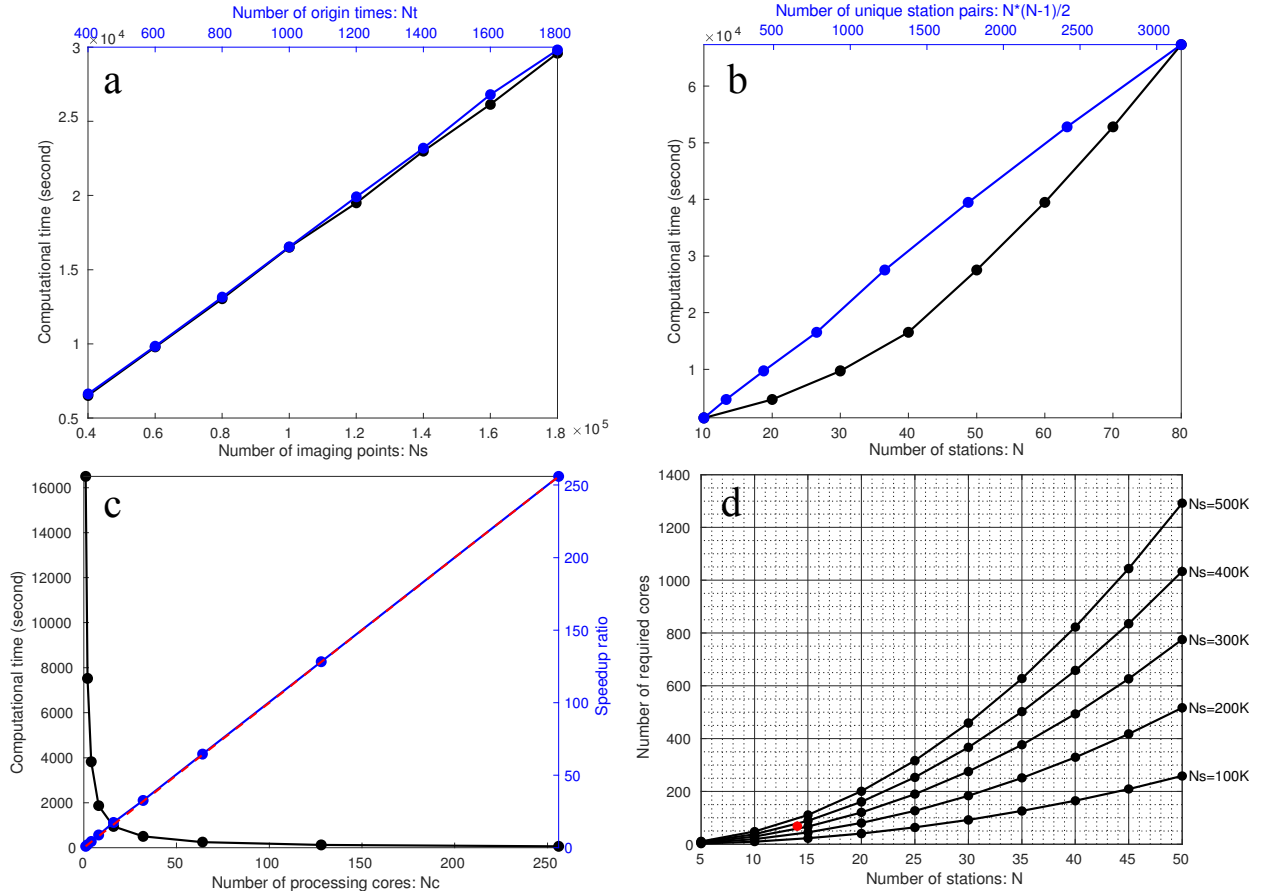


**Figure 1.** Computational efficiency analysis of the MCM location. The efficiency test is performed on the Intel E5-2670(2.6GHz) processor. (a) The computational times for different numbers of imaging points and searched origin times. Black line and the bottom X-axis show the variation of computational times with the number of imaging points, when the number of origin times and stations are fixed as 1000 and 40. Blue line and the top X-axis show the variation of computational times with the number of origin times, when the number of imaging points and stations are fixed as 100000 and 40. (b) The computational times for different numbers of stations, when the number of origin times and imaging points are fixed as 1000 and 100000. Black line and the bottom X-axis show the variation of computational time with the number of stations. Blue line and the top X-axis show the variation of computational time with the number of unique station pairs. Program runs on one core for (a) and (b). (c) The computational times (black line and left Y-axis) and speedup ratios (blue line and right Y-axis) when different numbers of cores are used. Red dashed line show the theoretical speedup ratios. The number of origin times, imaging points and stations are fixed as 1000, 100000 and 40. (d) The required cores used for real time processing under different numbers of stations and imaging points. Different black lines show the scenarios for different numbers of imaging points. The red dot shows the scenario for the following Uturuncu dataset, where 14 stations are deployed, 283556 imaging points are scanned and 68 cores are required for real time processing.



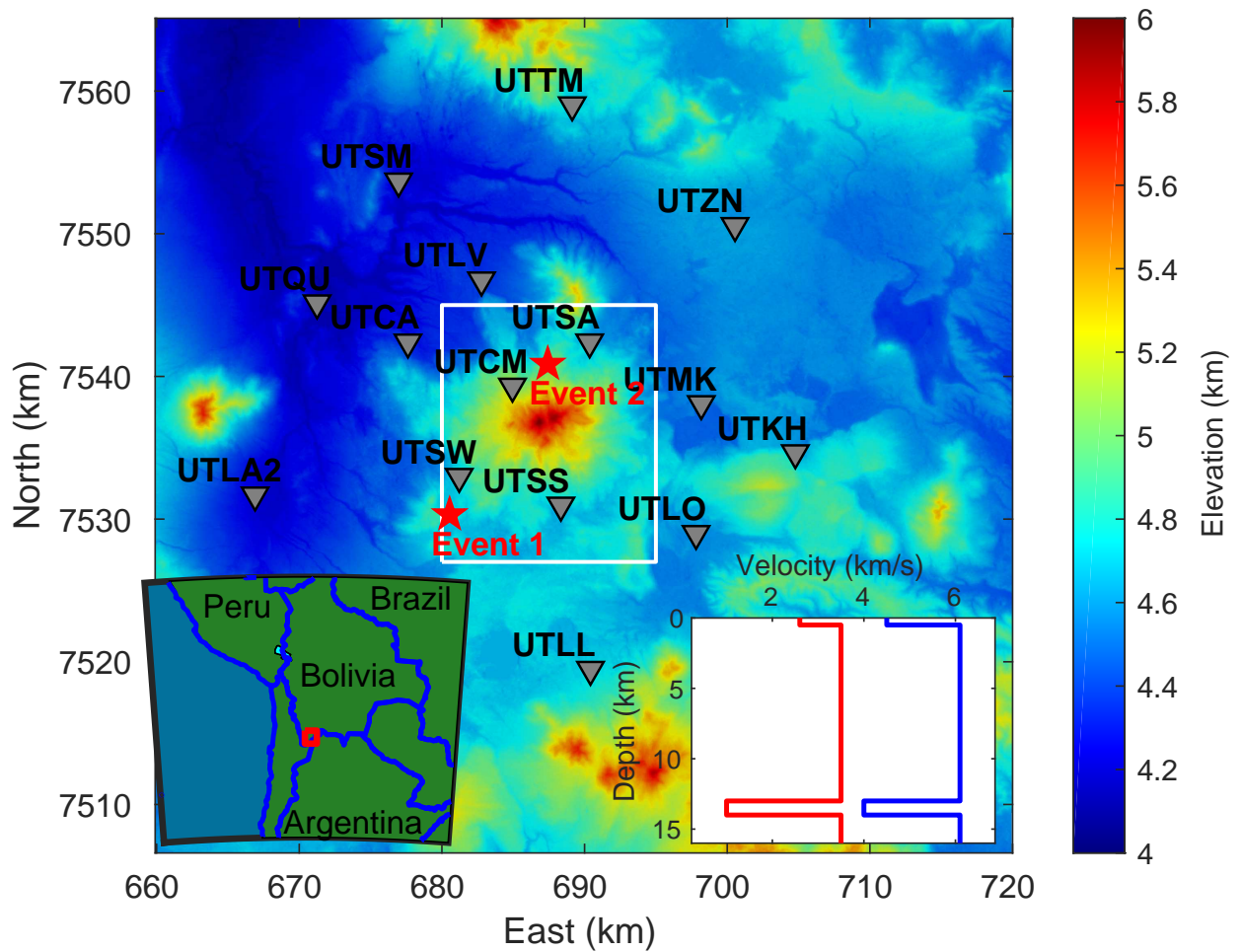


**Figure 2.** Location of the seismic stations and Uturuncu volcano (UTM zone: 19K). The stations are represented by gray triangles. Two local volcano-tectonic earthquakes in the catalogue are represented by red stars. The Uturuncu is located in the middle of the figure. The color in the figure represents elevation relative to the sea level. The lower left part exhibits a regional map, in which the red rectangle shows the research area. The lower right part exhibits the velocity model used in the event location, in which the red and blue lines show the P- and S-wave velocities. The white rectangle shows the imaging area (shown as Figure 11) for the four hours of continuous data.

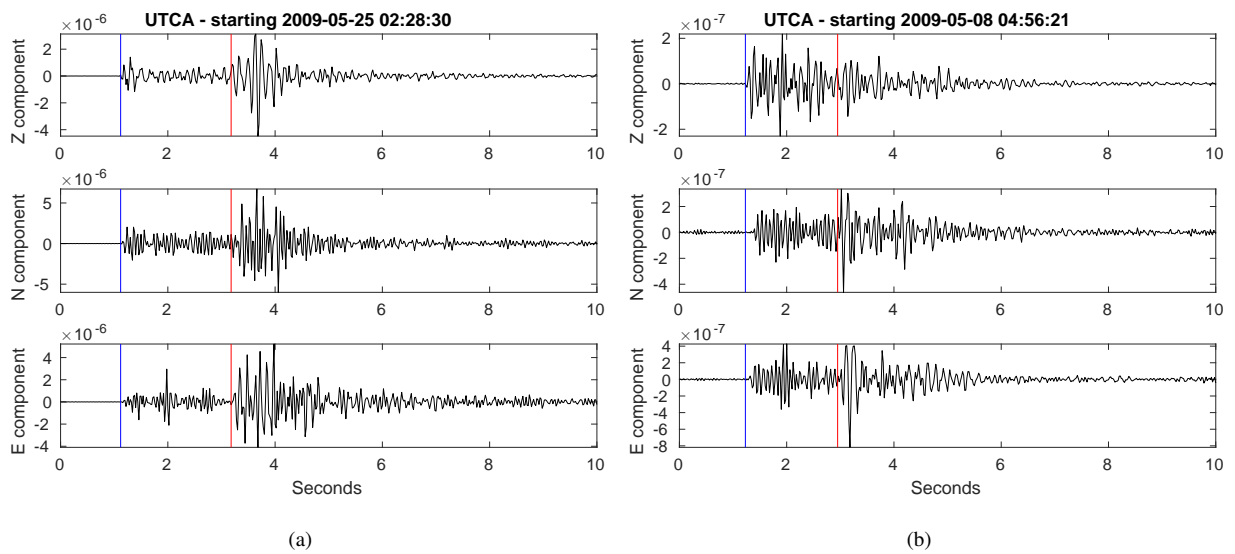


**Figure 3.** The recorded three component waveforms at station UTCA for the two shallow, local volcano-tectonic earthquake. The blue and red lines show the arrivals of P- and S-waves respectively. (a) Waveforms for the first event. The instrument response has been removed and the waveforms are filtered using a band-pass filter of 5-23 Hz. (b) Waveforms for the second event. The instrument response has been removed and the waveforms are filtered using a bandpass filter of 5-21 Hz.

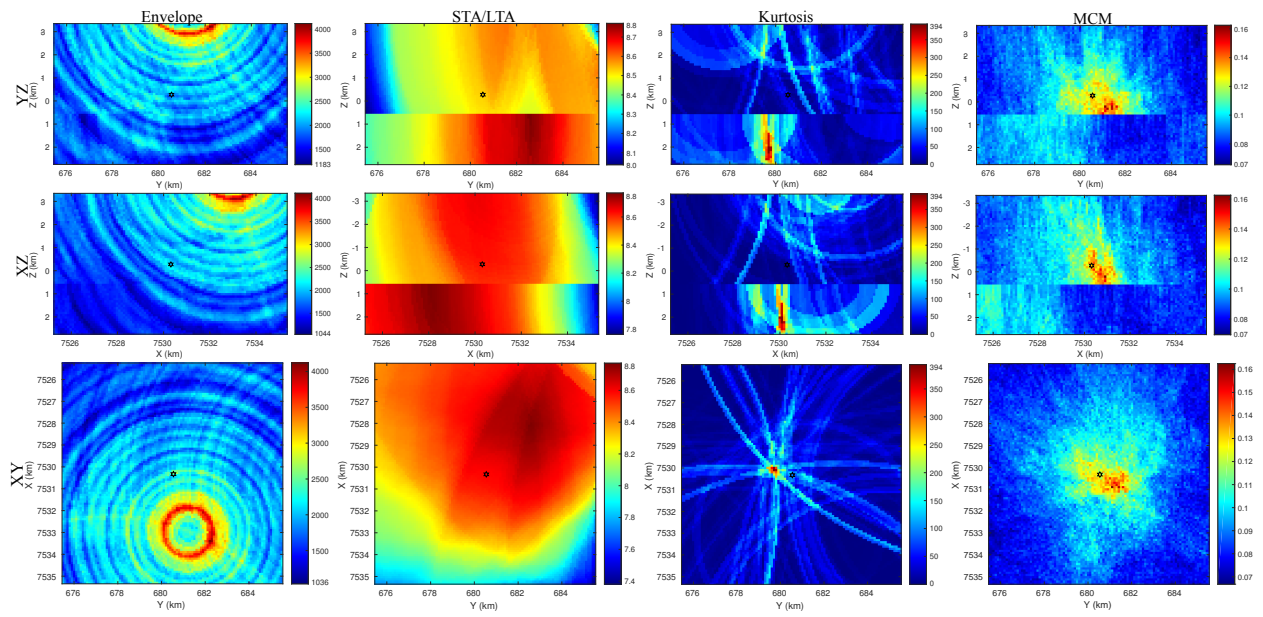


**Figure 4.** Migration profiles through the maximum migrated value for the first volcano-tectonic earthquake. The dark stars show the corresponding seismic event in the catalogue obtained by manual picking. The first column shows results of envelope, second column for STA/LTA, third column for kurtosis, fourth column for MCM. The first row shows YZ profiles, second row shows XZ profiles, third row shows XY profiles.

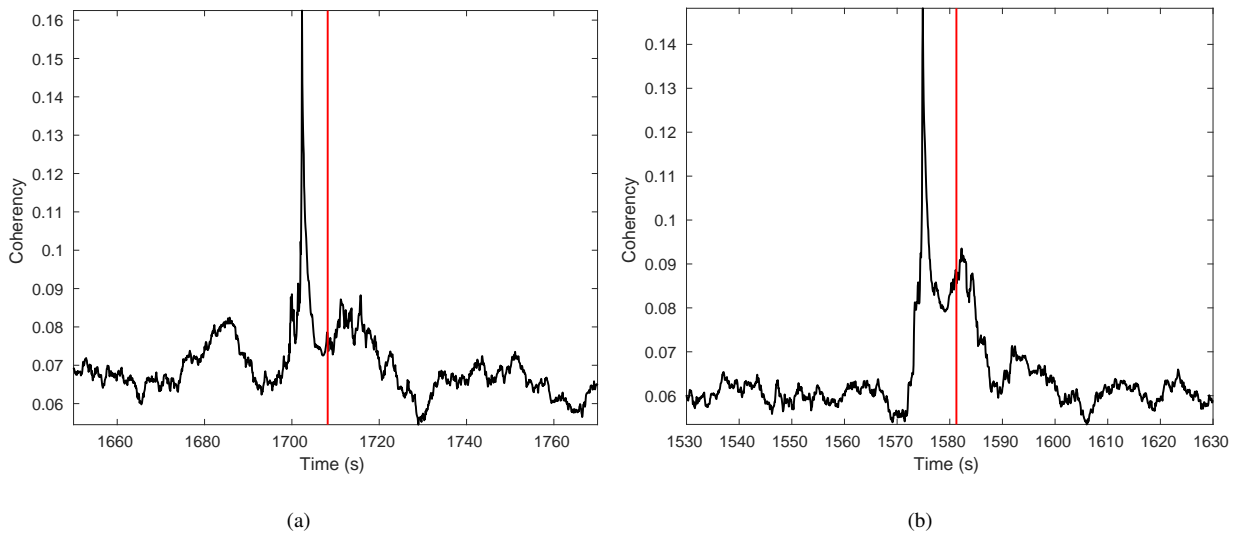


**Figure 5.** The stacking functions of the MCM method at the position of the maximum migrated value. The red line shows the origin time of the event in the catalogue obtained by manual picking. (a) The stacking function for event 1. The time is relative to 2009-05-25 02:00:00. (b) The stacking function for event 2. The time is relative to 2009-05-08 04:30:00.

**Table 1.** Location results of different waveform migration methods for the Uturuncu shallow volcano-tectonic earthquake and comparison with the event in the catalogue. The origin time is relative to 2009-05-25 02:00:00 (UTC).

	Event location				Deviation from manual traveltime location			
	X (km)	Y (km)	Z (km)	$T_0$ (s)	$\Delta X$ (m)	$\Delta Y$ (m)	$\Delta Z$ (m)	$\Delta T_0$ (s)
Catalogue	7530.316	680.543	-0.269	1708.2	-	-	-	-
Envelope	7533.4	682.2	-3.2	1709.8	3084	1657	2931	1.6
STA/LTA	7528.0	682.6	1.0	1709.4	2316	2057	1269	1.2
Kurtosis	7530.1	679.7	2.0	1708.4	216	843	2269	0.2
Coherency	7530.9	681.1	0.2	1708.3	584	557	469	0.1

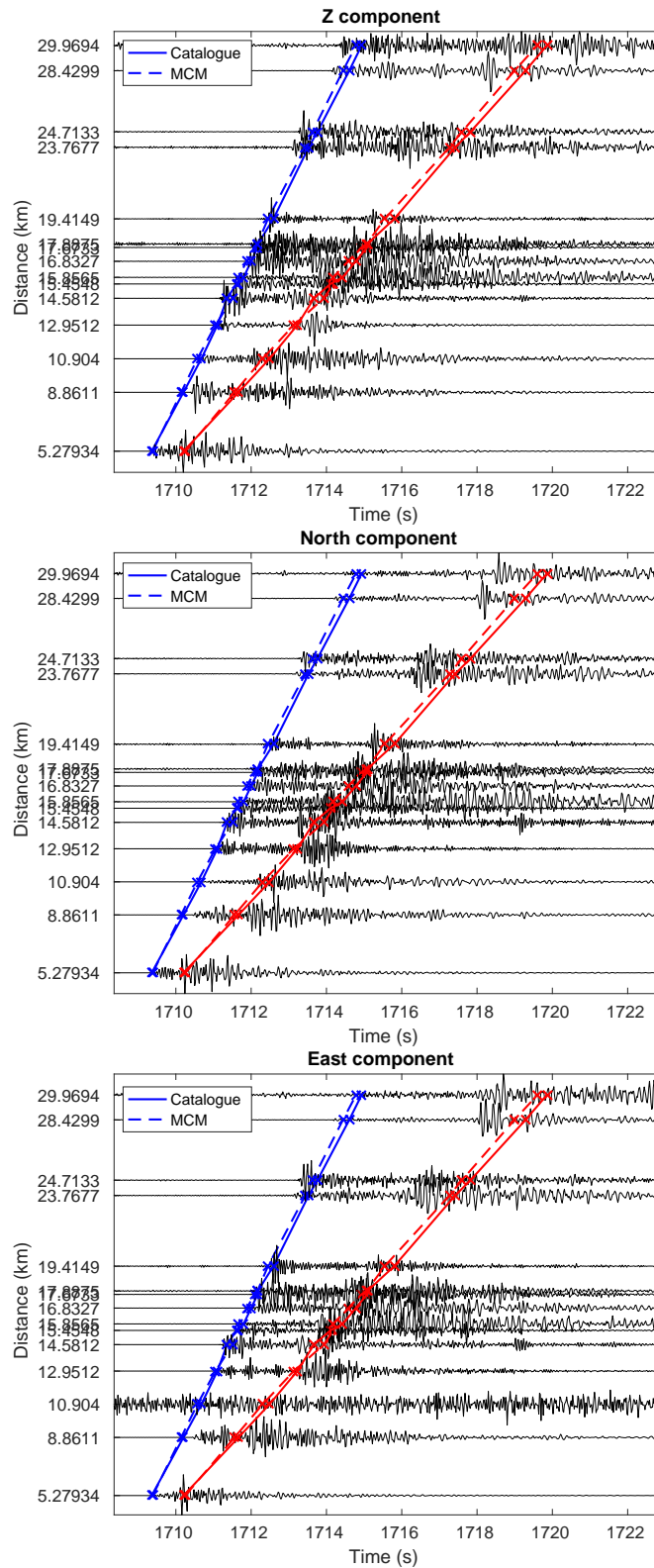


**Figure 6.** The three component record sections of the first event. The predicted P- and S-wave arrival times for this event in the catalogue and the event located by MCM are marked by solid and dashed lines respectively. The blue and red colors show the arrival times of the direct P- and S-wave respectively. The time in the figure is relative to 2009-05-25 02:00:00 (UTC).

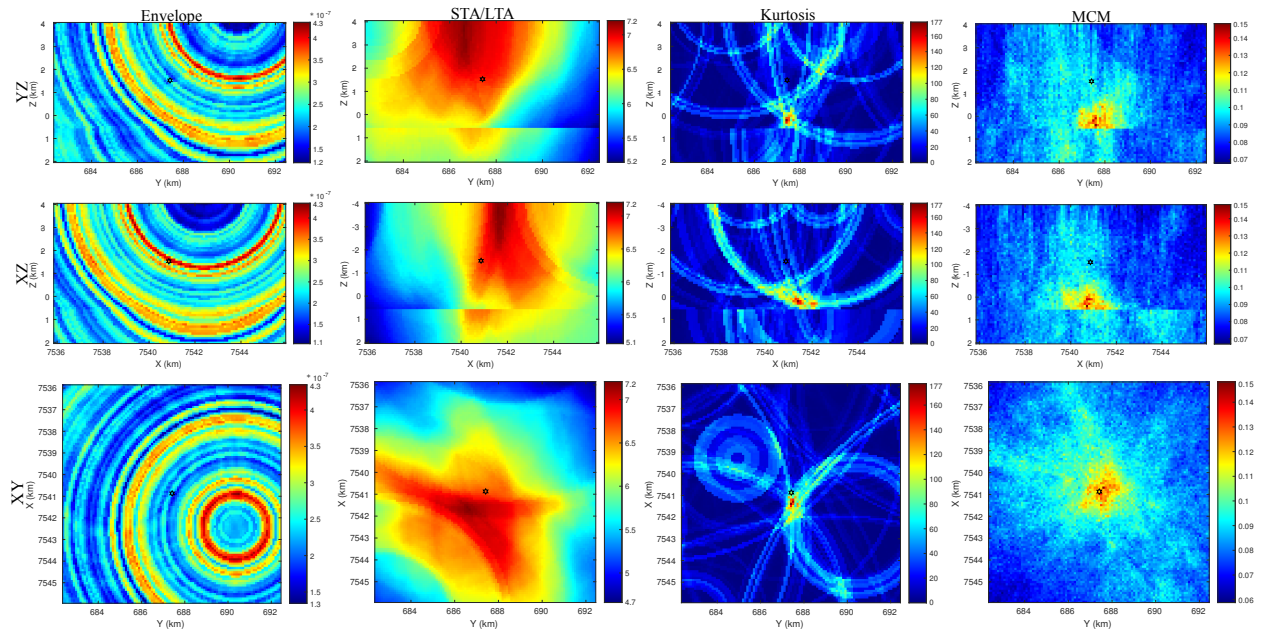


**Figure 7.** Migration profiles through the maximum migrated value for the second volcano-tectonic earthquake. The dark stars show the corresponding seismic event in the catalogue obtained by manual picking. The first column shows results of envelope, second column for STA/LTA, third column for kurtosis, fourth column for MCM. The first row shows YZ profiles, second row shows XZ profiles, third row shows XY profiles.

**Table 2.** Location results of different waveform migration methods for the Uturuncu shallow volcano-tectonic earthquake and comparison with the event in the catalogue. The origin time is relative to 2009-05-08 04:30:00 (UTC).

	Event location				Deviation from manual traveltime location			
	X (km)	Y (km)	Z (km)	$T_0$ (s)	$\Delta X$ (m)	$\Delta Y$ (m)	$\Delta Z$ (m)	$\Delta T_0$ (s)
Catalogue	7540.866	687.419	-1.523	1581.3	-	-	-	-
Envelope	7540.9	690.5	-1.6	1582.2	34	3081	77	0.9
STA/LTA	7541.6	686.6	-3.6	1582.9	734	819	2077	1.6
Kurtosis	7541.4	687.4	0.2	1580.9	534	19	1723	0.4
Coherency	7540.7	687.6	0.4	1580.7	166	181	1923	0.6



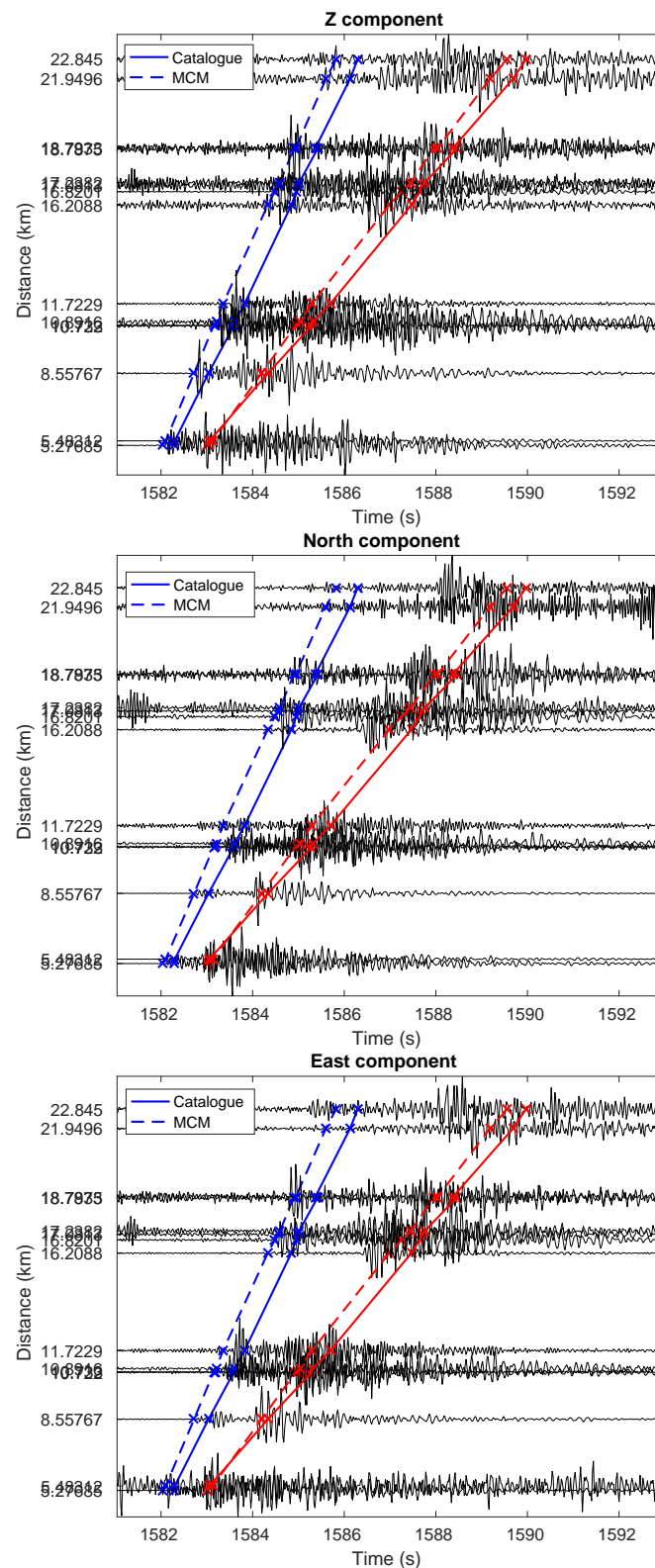


**Figure 8.** The three component record sections of the second event. The predicted P- and S-wave arrival times for this event in the catalogue and the event located by MCM are marked by solid and dashed lines respectively. The blue and red colors show the arrival times of the direct P- and S-wave respectively. The time in the figure is relative to 2009-05-08 04:30:00 (UTC).

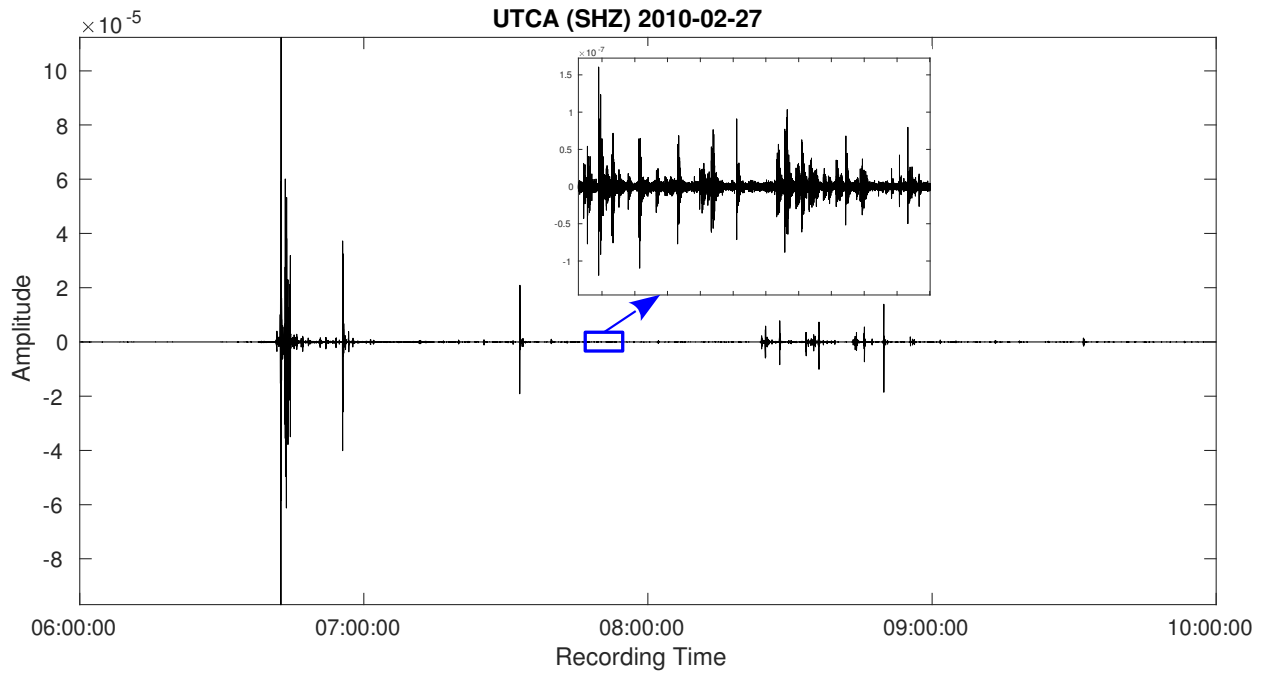


**Figure 9.** The recorded Z component waveforms at station UTCA. The recording time ranges from 06:00:00 to 10:00:00 (UTC). The waveforms within the blue rectangle are enlarged. The instrument response has been removed and the waveforms are filtered using a bandpass filter of 4.2-21.6 Hz.

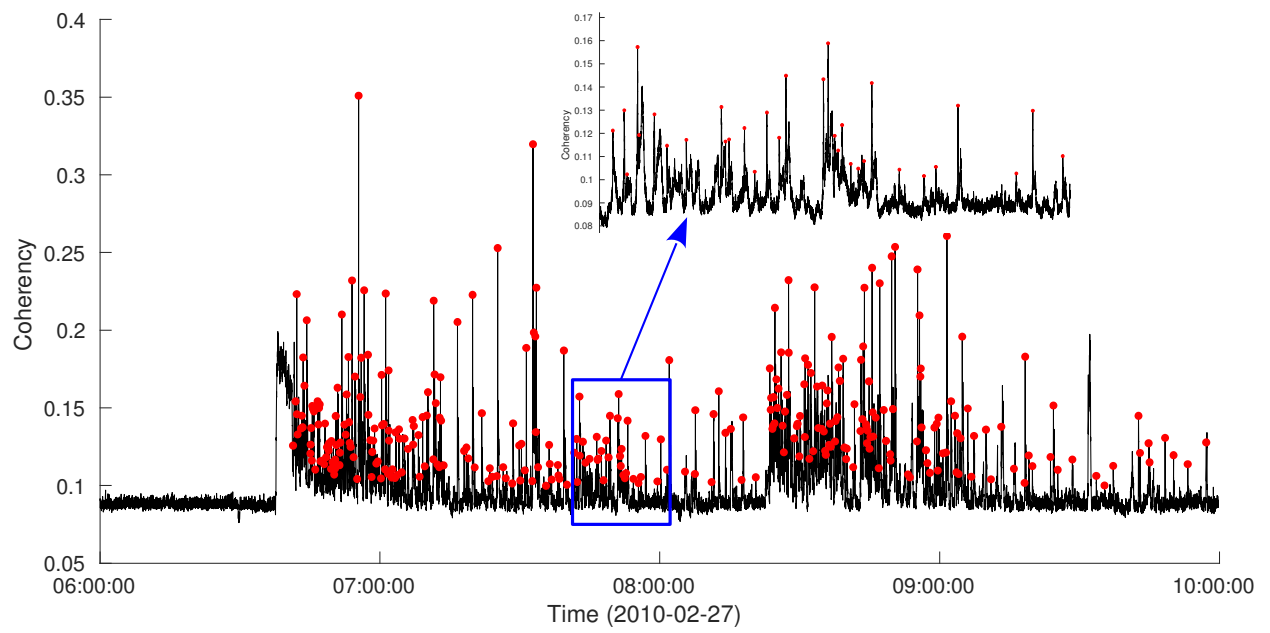


**Figure 10.** The maximum coherency value at each searched origin time for the four hours of continuous data. The time interval is 0.08 s. The part in the blue rectangle is enlarged. The red points show the 322 verified seismic events.

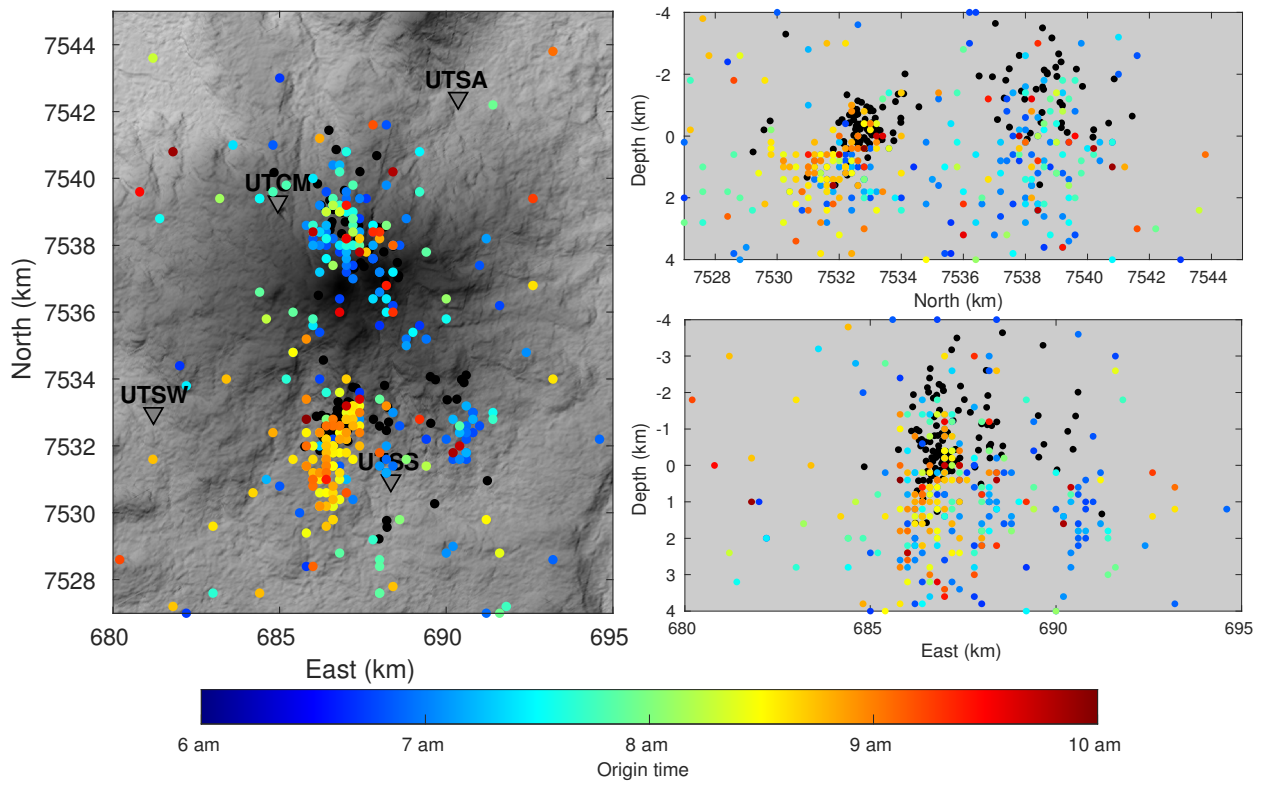


**Figure 11.** The earthquake locations on the horizontal and vertical profiles. Black dots show the 114 event locations in the existing catalogue. The color-coded dots show the verified 322 event locations for the MCM. The color represents the origin times of earthquake events.

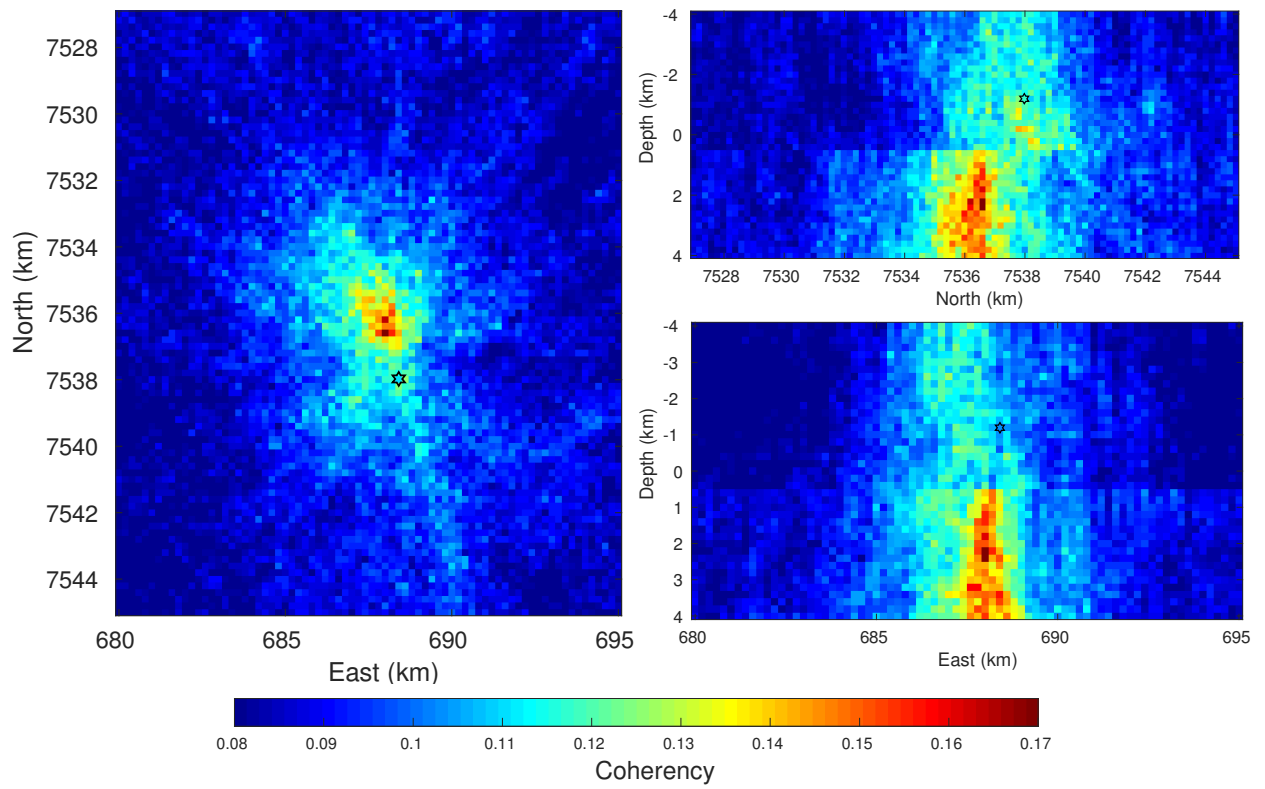


**Figure 12.** Horizontal and vertical profiles at the maximum value of the migration volume for seismic event 1. Color represents the migration value (coherency). Black star represents the event location in the catalogue.

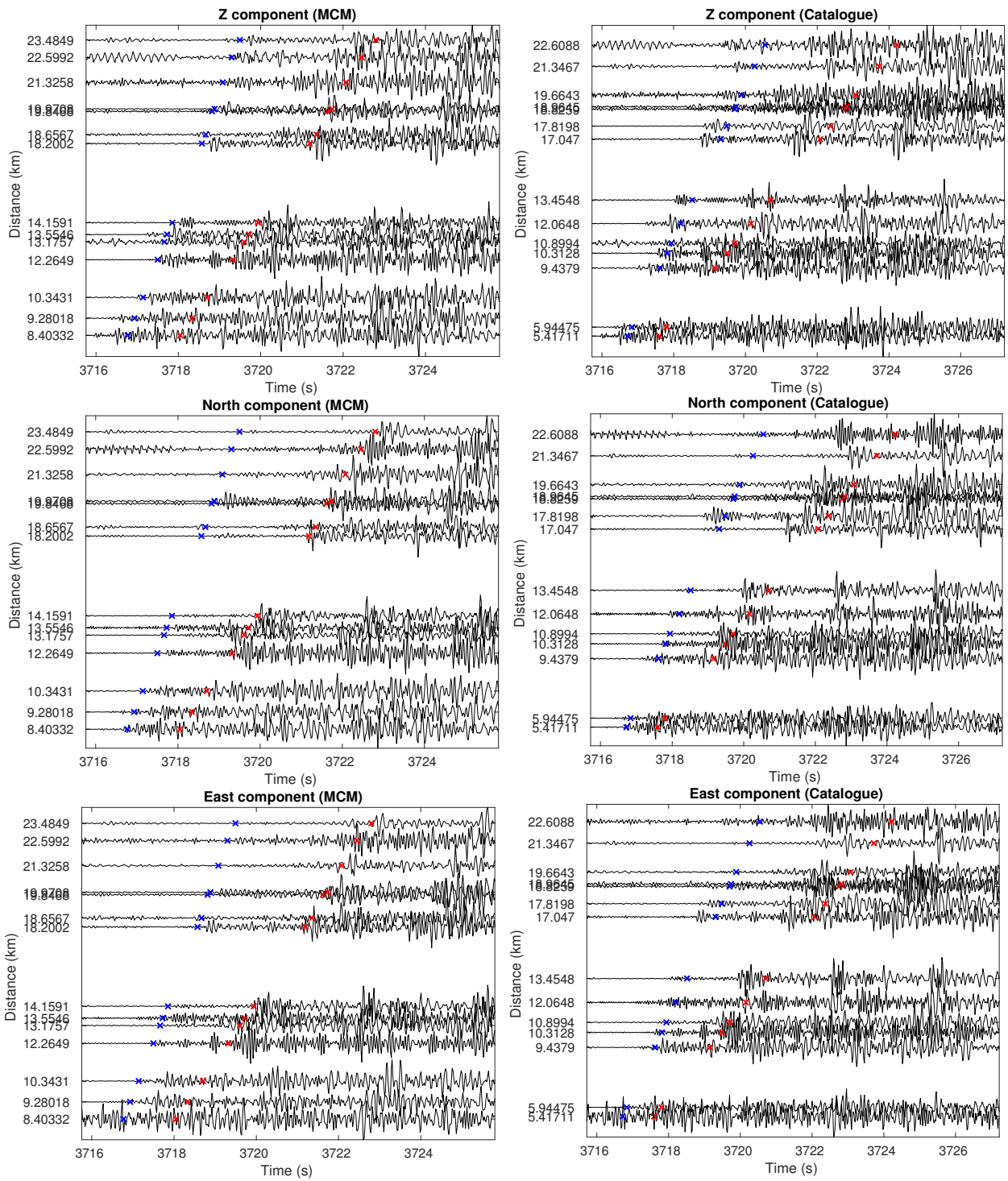


**Figure 13.** Three component record sections for seismic event 1. The predicted P- and S-wave arrival times are marked by blue and red crosses, respectively. Left panel: record sections for the MCM location result. Right panel: record sections for the catalogue location result. The time in the figure is relative to 2010-02-27 06:00:00 (UTC).

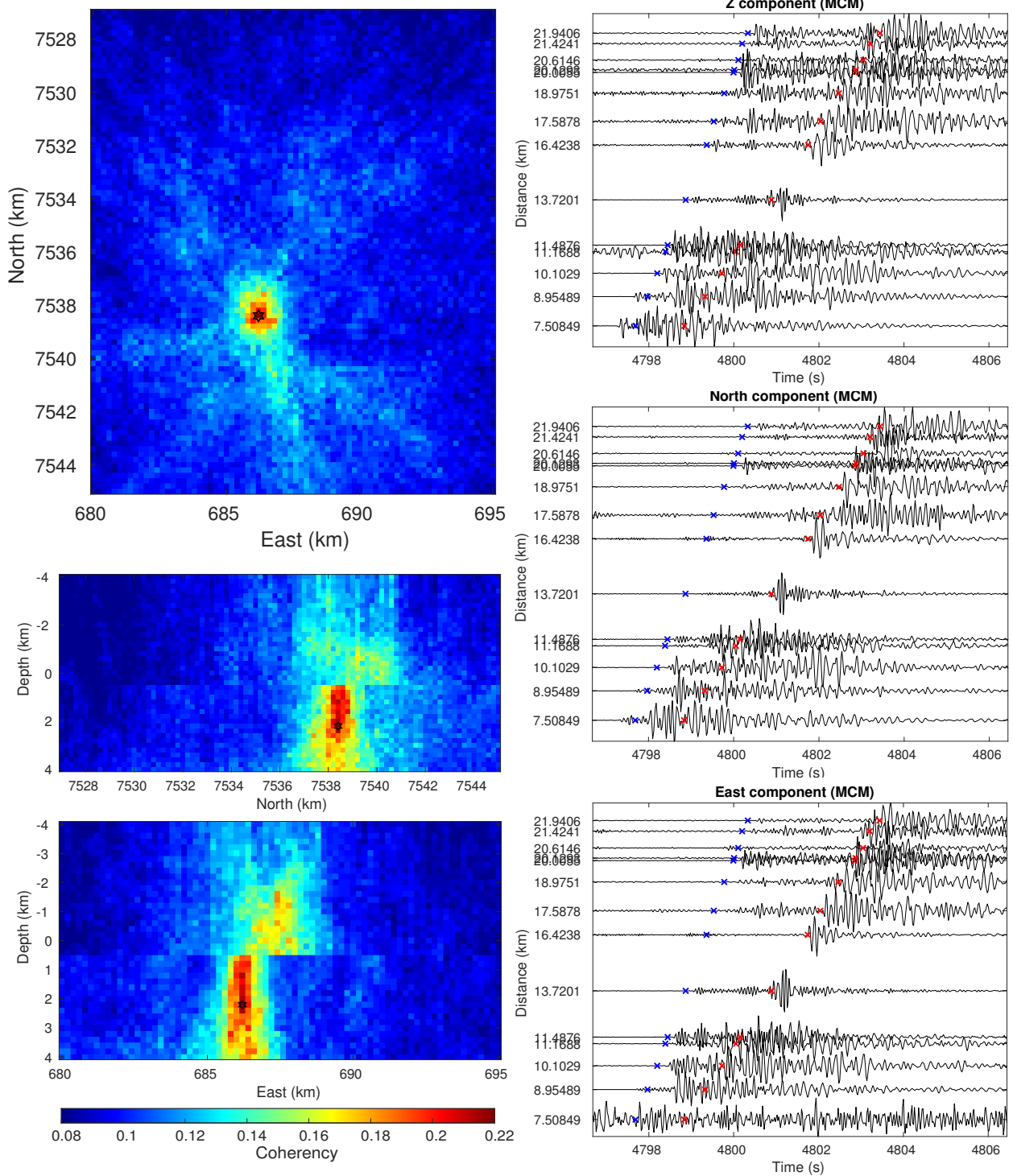


**Figure 14.** Horizontal and vertical migration profiles and three component record sections for seismic event 2, which is newly detected by MCM and not in the existing catalogue. The predicted P- and S-wave arrival times are marked by blue and red crosses on the record sections, respectively. Left panel: horizontal and vertical profiles at the maximum value of the migration volume. Color represents the migration value and black star shows the final event location. Right panel: record sections for this event.

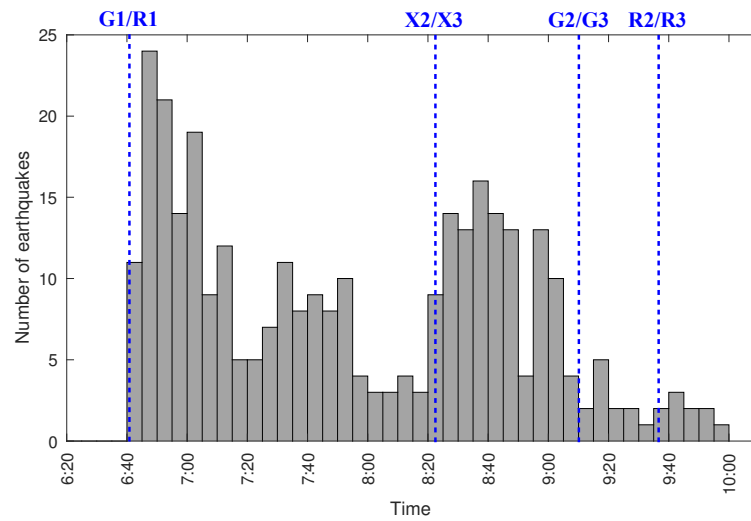


**Figure 15.** Histogram of UTURUNCU triggered events from the  $M_w$  8.8 Maule earthquake for the four hours (6 am to 10 am) in 5-min bins. There are no seismic events from 6:00 am to 06:40 am. Blue dashed lines show the approximate arrival time of surface wave trains. G1/R1 represents the minor-arc Love (G1) and Rayleigh (R1) waves. X2/X3, G2/G3 and R2/R3 represent different surface wave overtones (Jay et al. 2012).



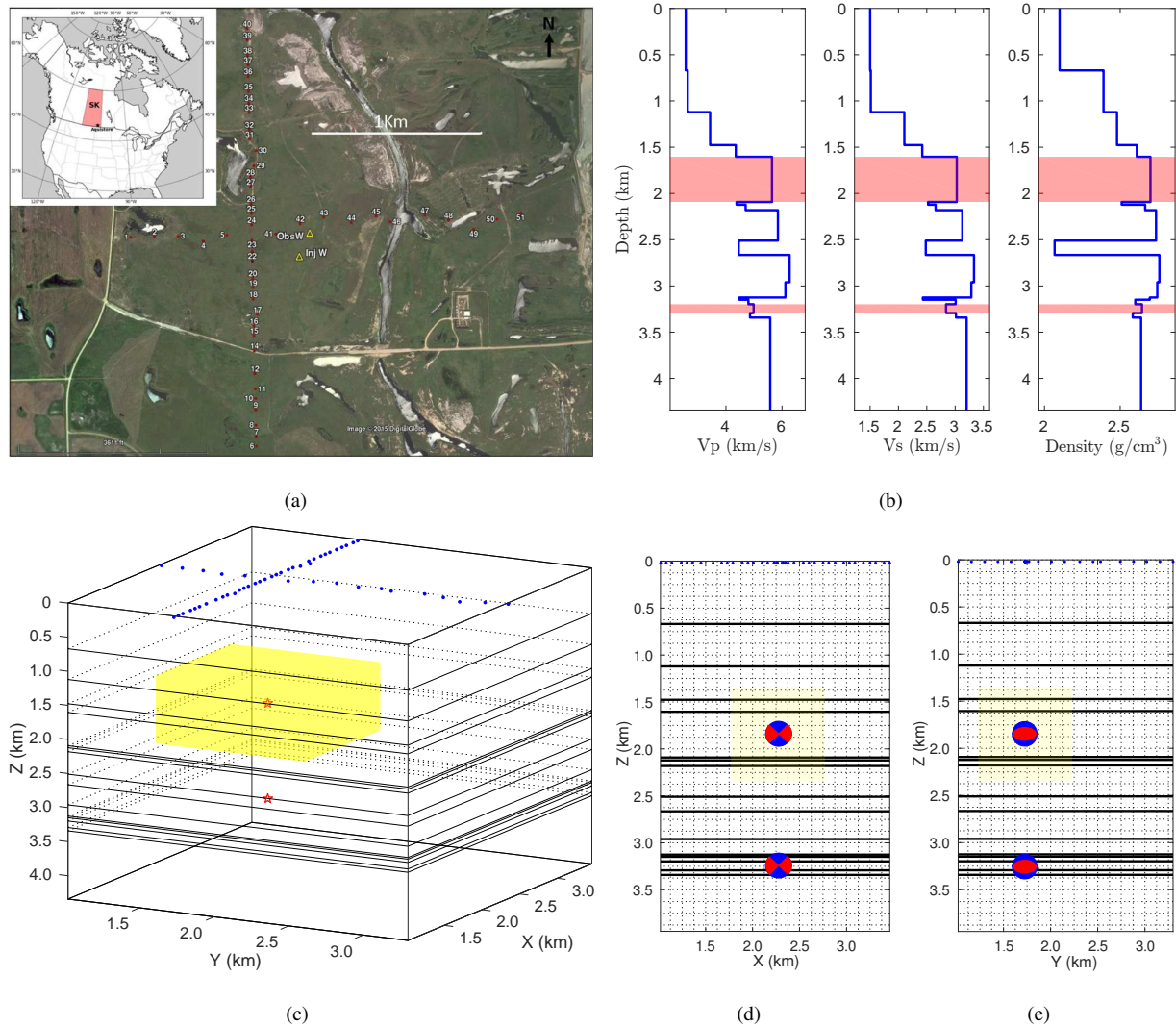


**Figure 16.** (a) Aquistore permanent seismic array geometry. Geophones are denoted by red dots alongside the station number, while the observation and injection wells are illustrated by yellow triangles. (From Birnie et al. (2016)). (b) P- and S-wave velocity model and density model in Aquistore area. The red color highlights two target layers where the seismic events are located. (c) The numerical model space of the Aquistore area. Vertical (d) XZ and (e) YZ profiles of the numerical model. The red stars shows the locations of two seismic events, whose depth are 1.85 km and 3.25 km respectively. Blue points represent the surface geophones. The yellow color exhibits the imaging area of the shallow event. Source radiation patterns are shown in the vertical profiles using a beach ball with red and blue colors.

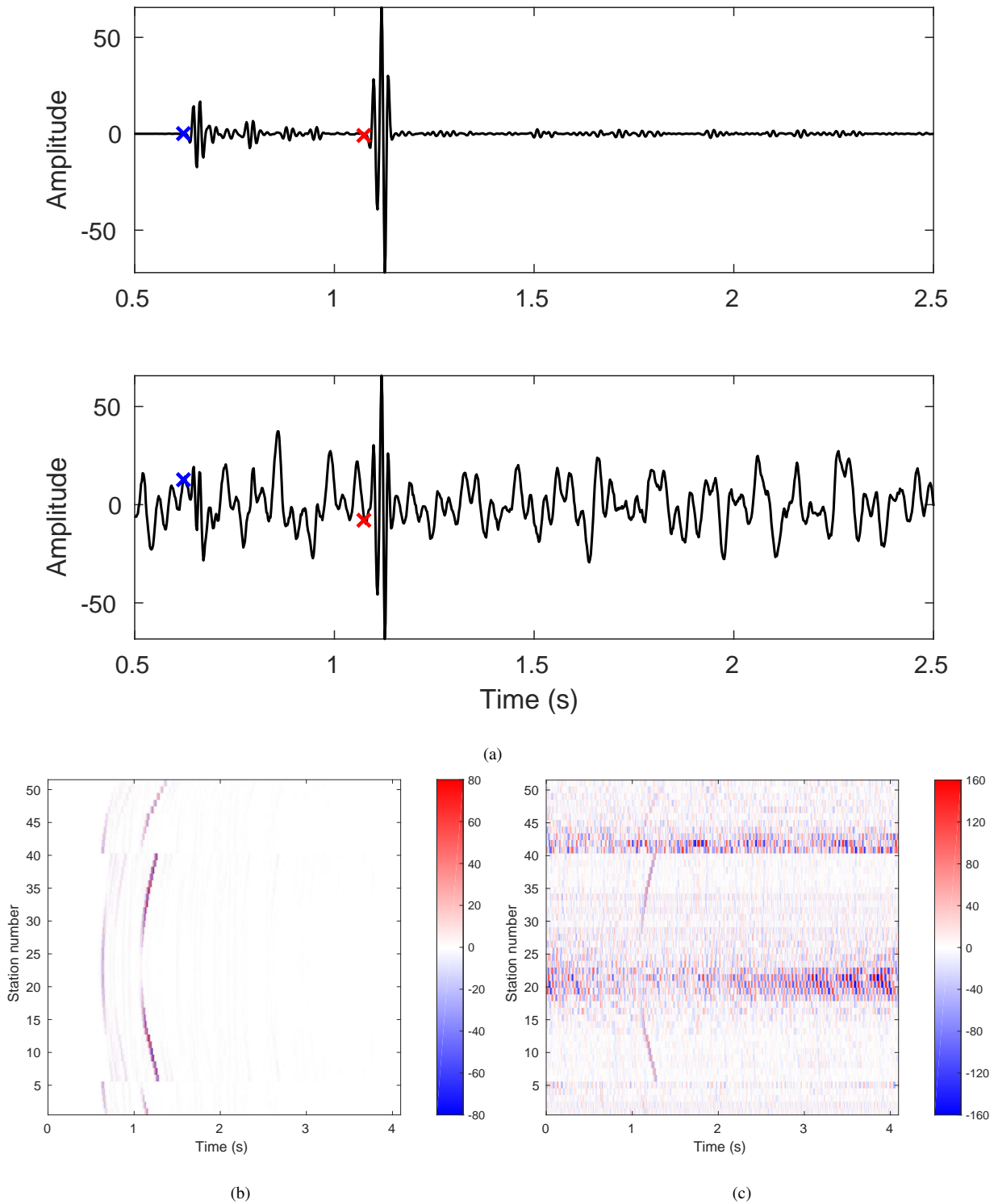


**Figure 17.** (a) The recorded waveform data at station 30 before (top) and after (bottom) adding real noise. The blue and red crosses show the arrivals of P- and S-phases. (b) The synthetic noise-free seismic profile. (c) The seismic profile after adding real noise. The SNR is 0.5.

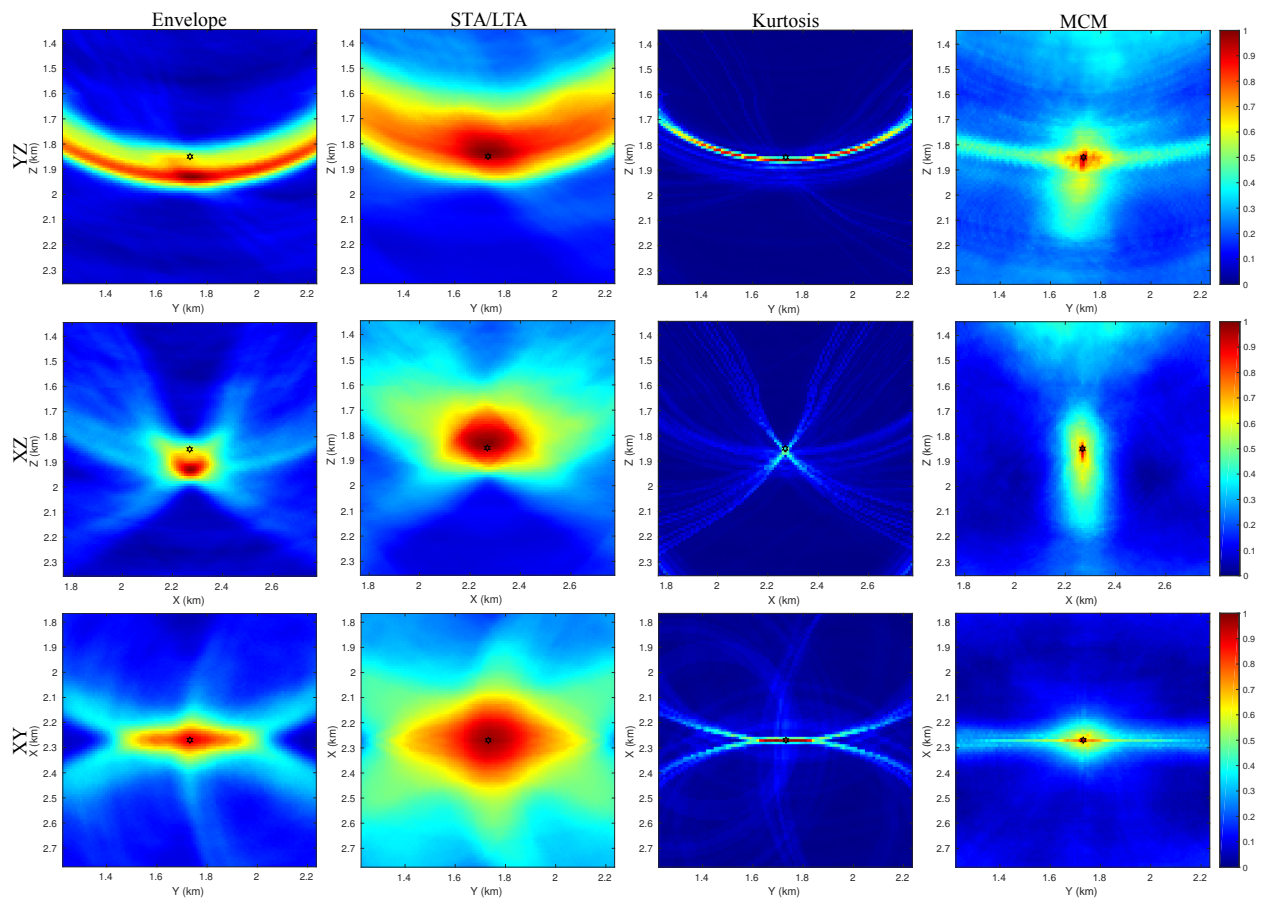


**Figure 18.** Profiles of the migration results through the true source location for the four methods. The SNR is 1. The dark star in the center shows the true source location. The first column shows results of envelope, second column for STA/LTA, third column for kurtosis, fourth column for MCM. The first row shows YZ profiles, second row shows XZ profiles, third row shows XY profiles.

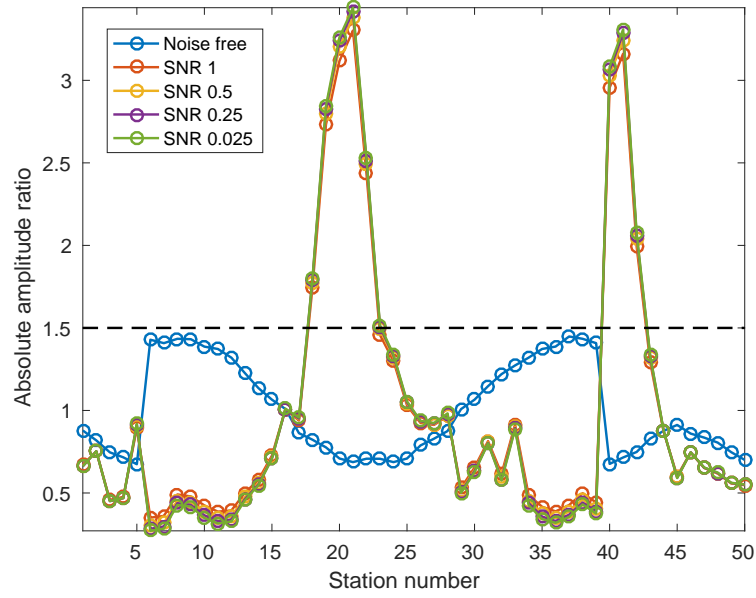


**Figure 19.** The absolute amplitude ratios for different stations under different SNR scenarios. The absolute amplitude ratio of different traces is defined as the ratio of the average absolute amplitudes of a trace to the average absolute amplitude of all traces. The black dashed line shows an absolute amplitude ratio of 1.5.

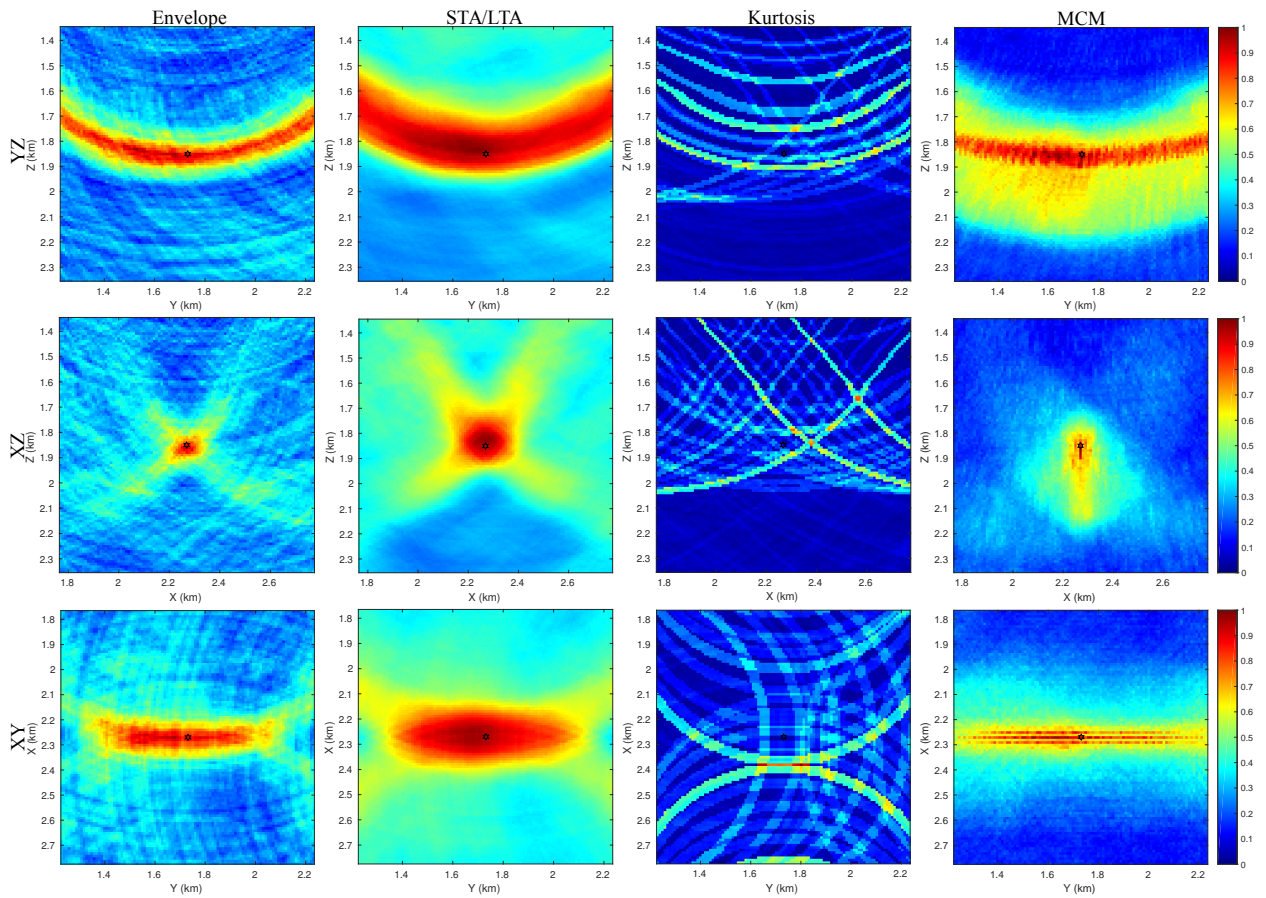


**Figure 20.** Profiles of the migration results through the true source location with automatic quality control scheme (weighting and filtering). The SNR is 0.025. The dark star in the center shows the true source location. The first column shows results of envelope, second column for STA/LTA, third column for kurtosis, fourth column for MCM. The first row shows YZ profiles, second row shows XZ profiles, third row shows XY profiles.

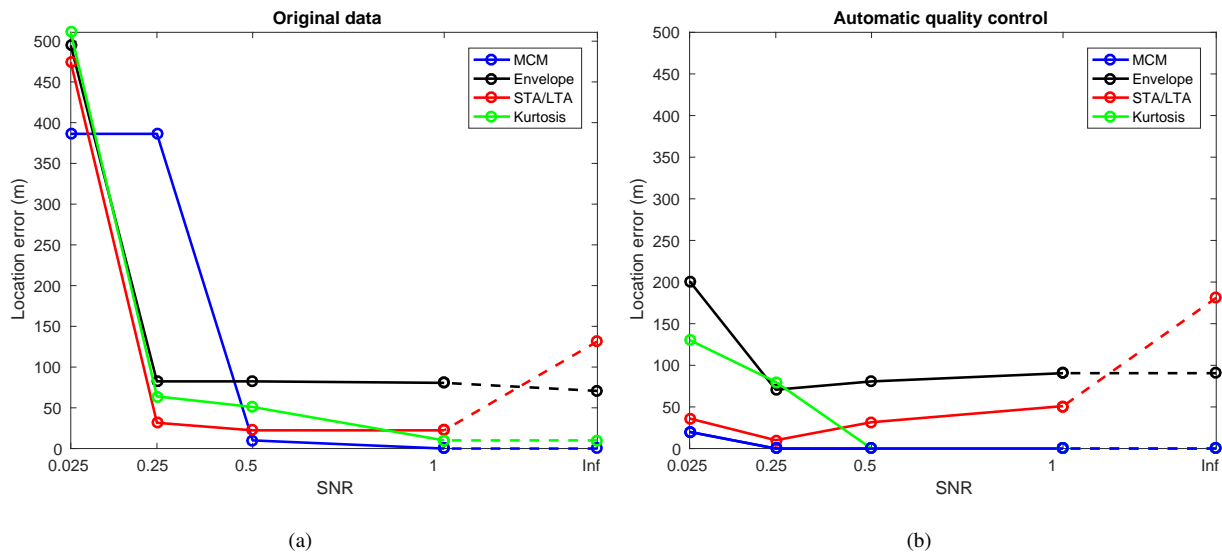


**Figure 21.** The location errors of the four methods under different SNRs with (a) original data and (b) automatic quality control scheme (weighting and filtering).

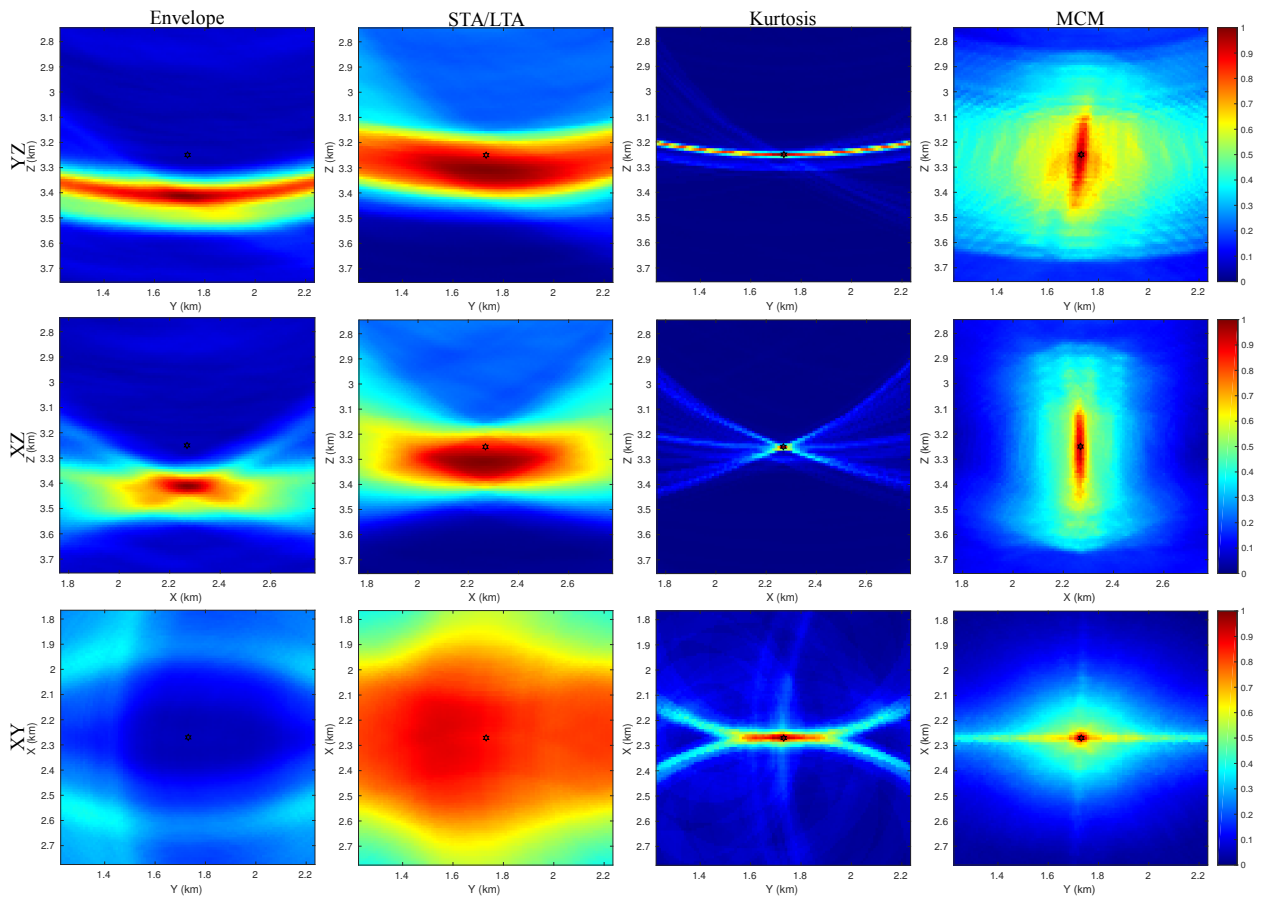


**Figure 22.** Migration profiles through the true source location of the deep event. The SNR is 1. The dark star in the center shows the true source location. The first column shows results of envelope, second column for STA/LTA, third column for kurtosis, fourth column for MCM. The first row shows YZ profiles, second row shows XZ profiles, third row shows XY profiles.

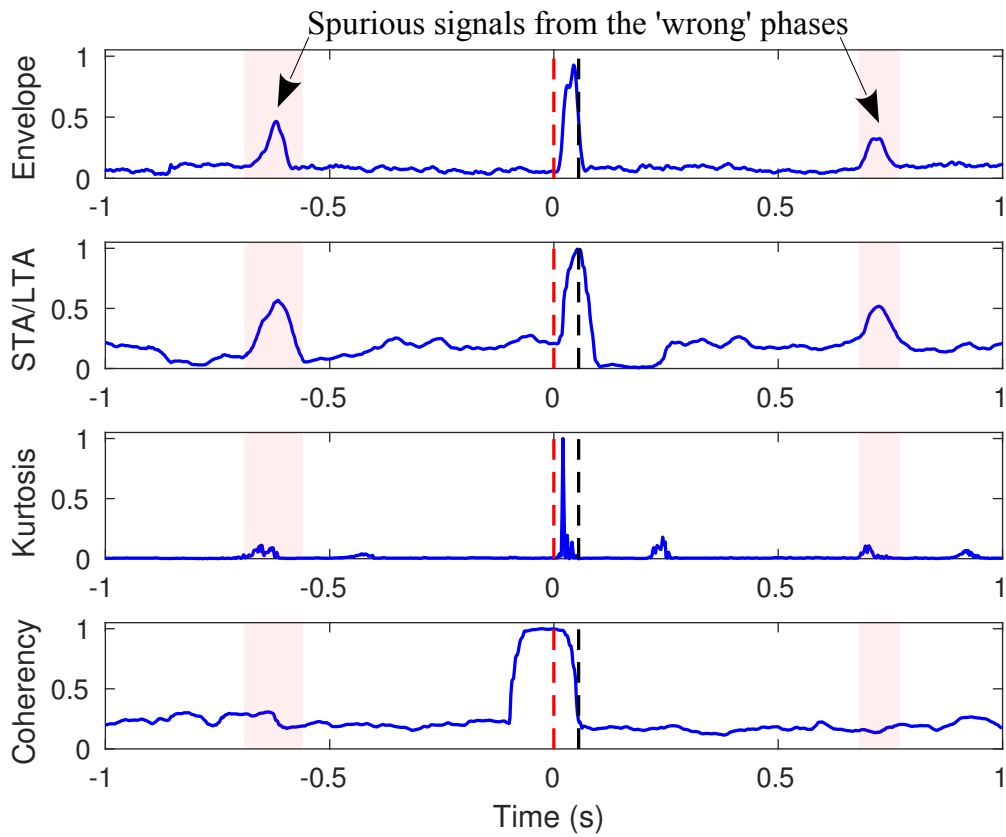


**Figure 23.** The stacking functions of the four methods at the true source location of the deep event for the Aquistore noise data. The red dashed lines show the origin time of the source time function and the black dashed lines show the end time of the source time function. The pink areas around -0.6 s and 0.7 s highlight the time range where P-/S-phases move into the stacking window of the S-/P-phases when searching for origin time. The SNR is 1.



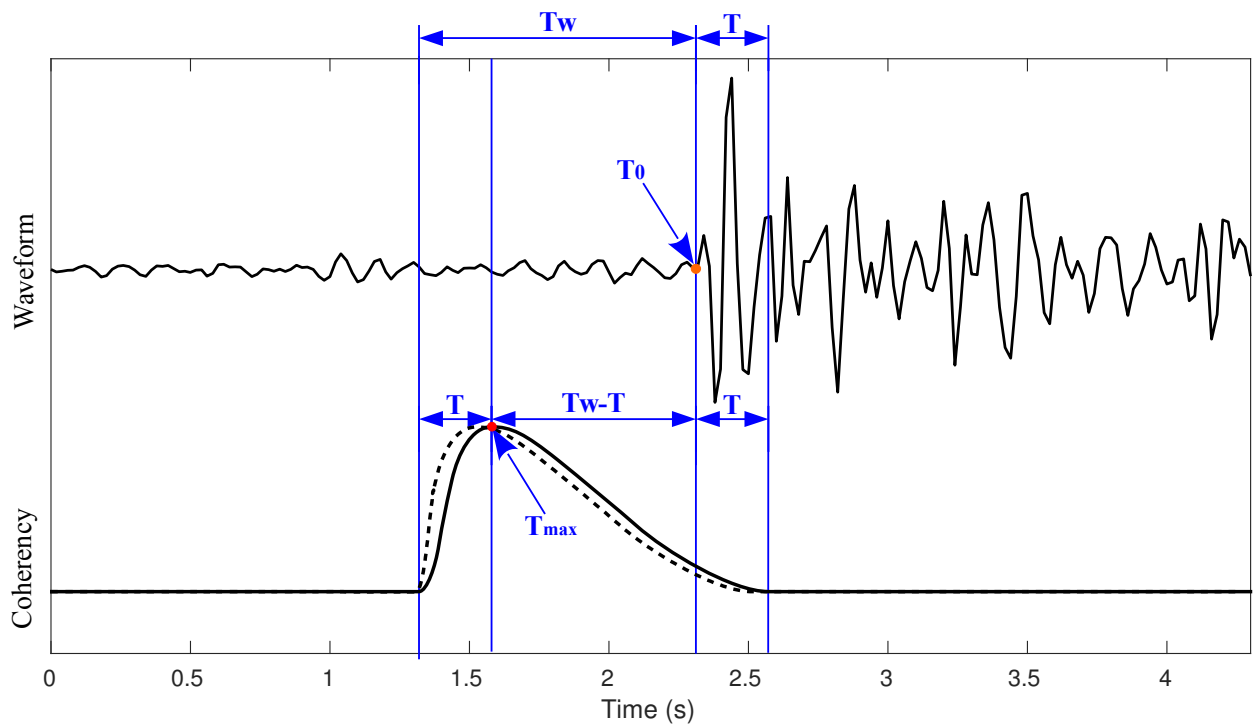


**Figure 24.** Schematic diagram showing recorded waveforms and the corresponding stacked coherency trace.  $T_w$  is the length of coherent analysis time window, and  $T$  is the period of direct wave. The orange dot shows the arrival time of direct wave, and the red dot shows the maximum coherency value at the stacked coherency trace. For the stacked coherency trace, the solid line shows the maximum coherency value appearing at  $T$  time after the rise of waveform coherency, and the dashed line shows the maximum coherency value appearing within  $T$  time after the rise of waveform coherency.

# Supplementary Materials

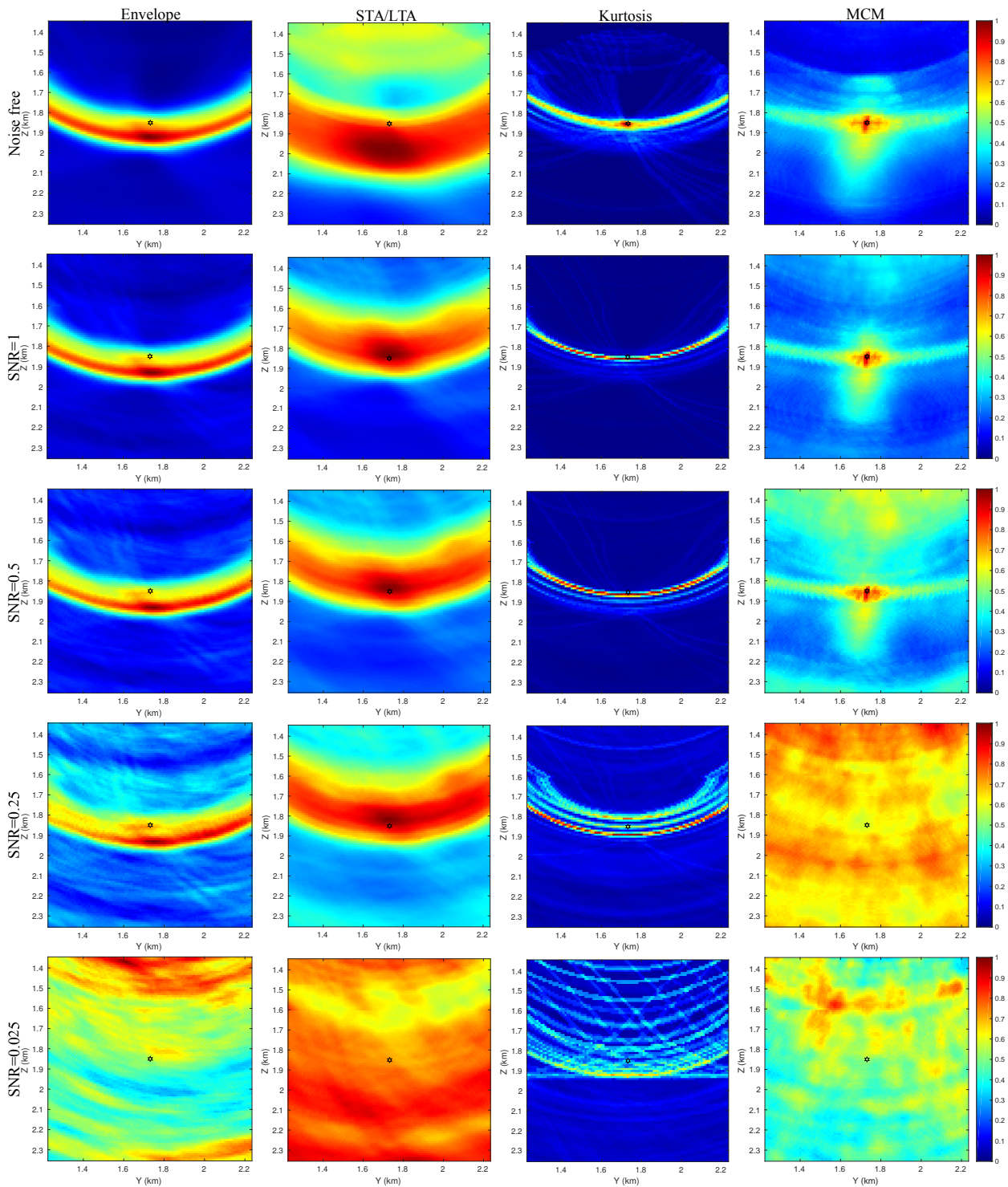


**Figure S.1.** Vertical profiles (YZ profiles) through the true source location of the migration results under different SNRs for the four methods. The dark star in the center shows the true source location. The first column shows results of envelope, second column for STA/LTA, third column for kurtosis, fourth column for MCM. The first row shows the results when data is free of noise, second row for SNR is 1, third row for SNR is 0.5, fourth row for SNR is 0.25, fifth row for SNR is 0.025.

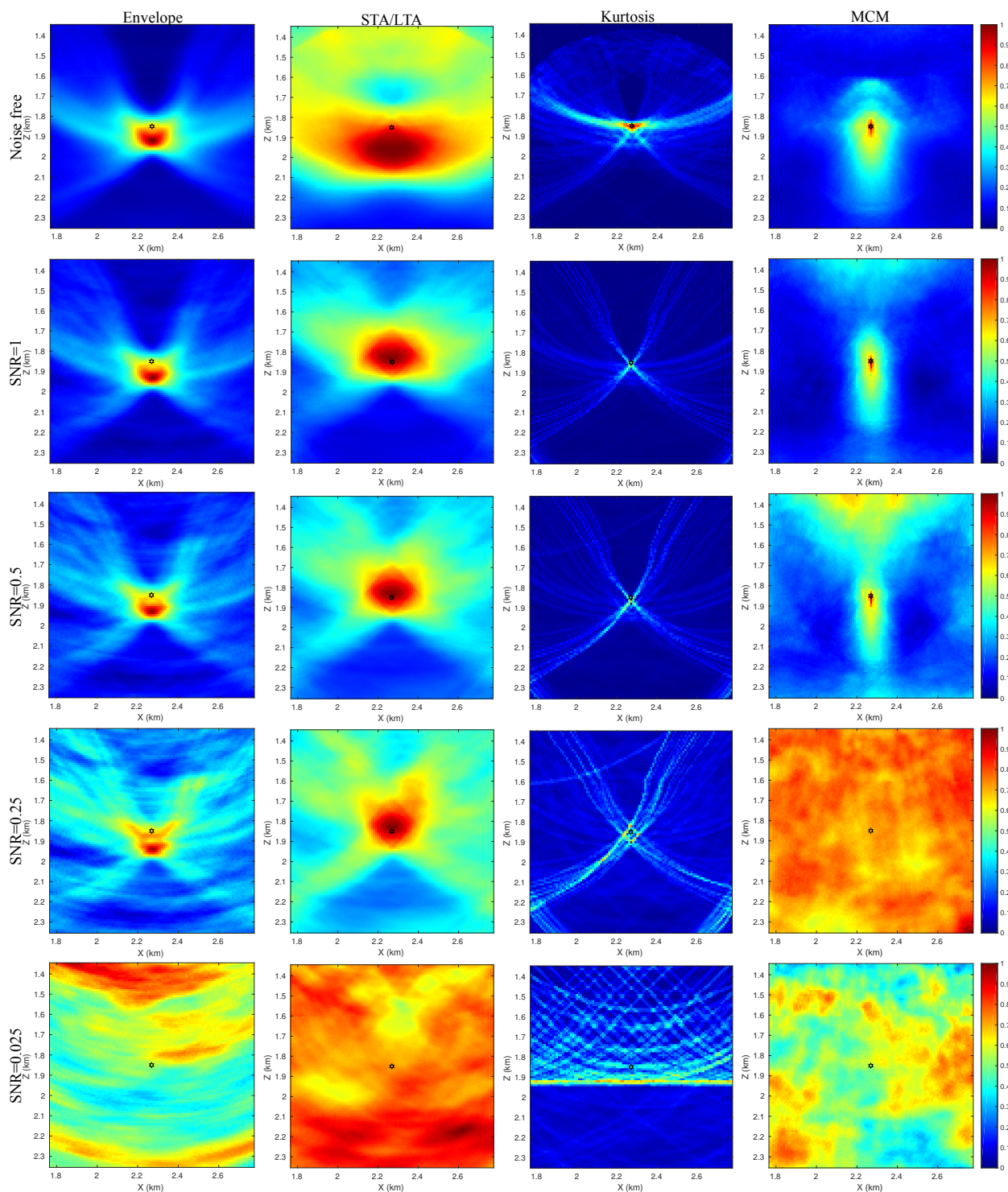


**Figure S.2.** Vertical profiles (XZ profiles) through the true source location of the migration results under different SNRs for the four methods. The dark star in the center shows the true source location. The first column shows results of envelope, second column for STA/LTA, third column for kurtosis, fourth column for MCM. The first row shows the results when data is free of noise, second row for SNR is 1, third row for SNR is 0.5, fourth row for SNR is 0.25, fifth row for SNR is 0.025.

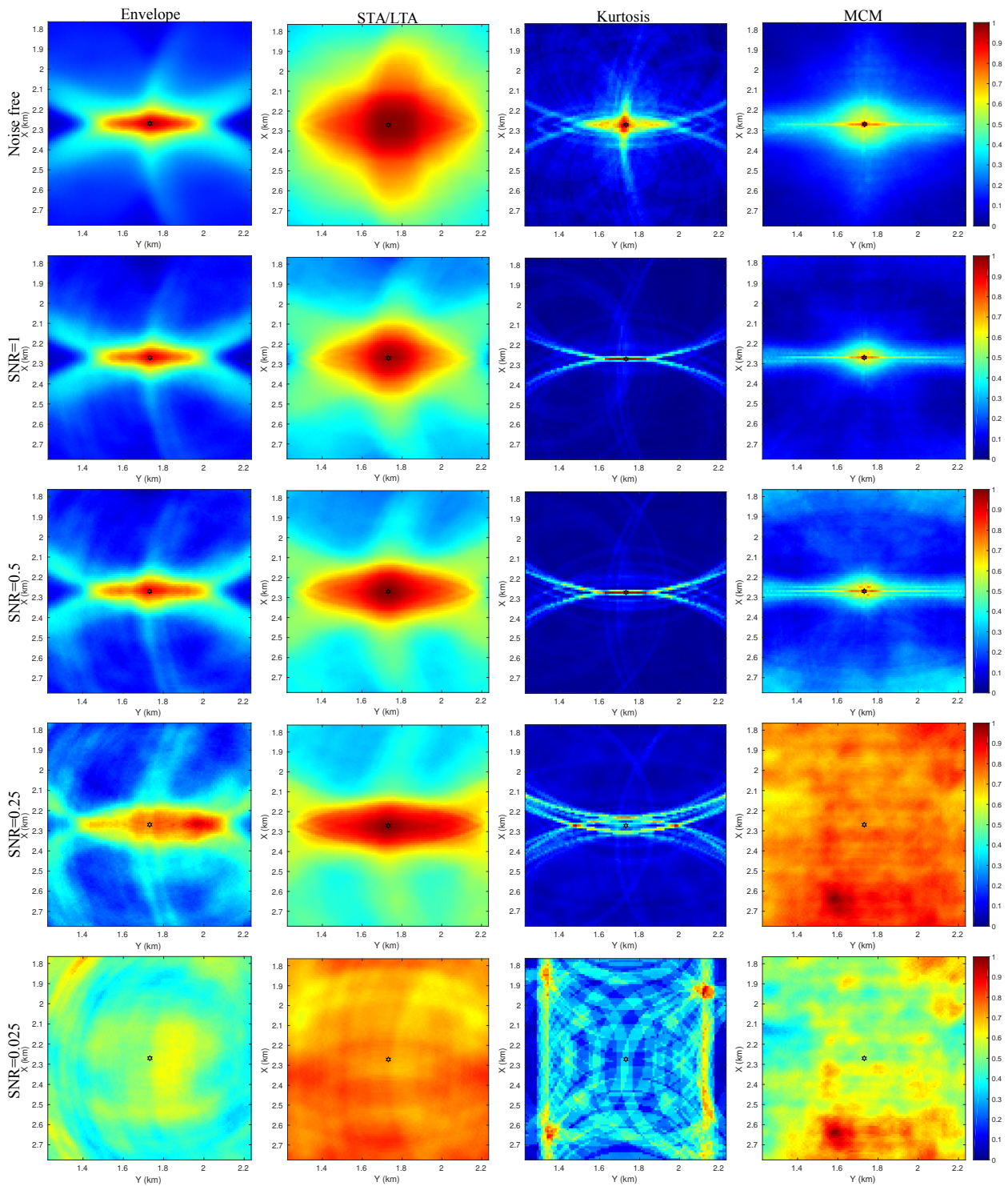


**Figure S.3.** Horizontal profiles (XY profiles) through the true source location of the migration results under different SNRs for the four methods. The dark star in the center shows the true source location. The first column shows results of envelope, second column for STA/LTA, third column for kurtosis, fourth column for MCM. The first row shows the results when data is free of noise, second row for SNR is 1, third row for SNR is 0.5, fourth row for SNR is 0.25, fifth row for SNR is 0.025.

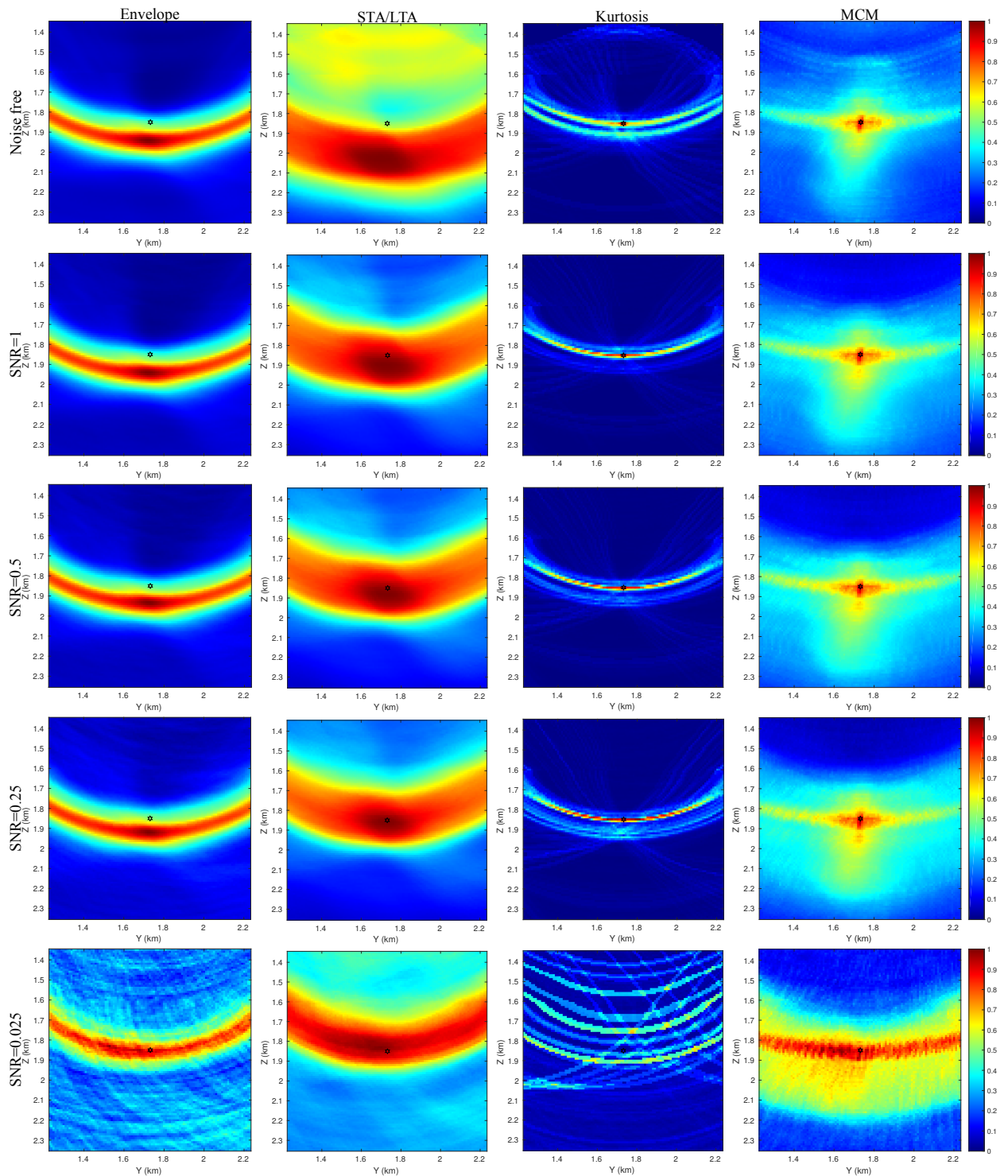


**Figure S.4.** Vertical profiles (YZ profiles) through the true source location of the migration results with automatic quality control scheme (weighting and filtering) under different SNRs. The dark star in the center shows the true source location. The first column shows results of envelope, second column for STA/LTA, third column for kurtosis, fourth column for MCM. The first row shows the results when data is free of noise, second row for SNR is 1, third row for SNR is 0.5, fourth row for SNR is 0.25, fifth row for SNR is 0.025.

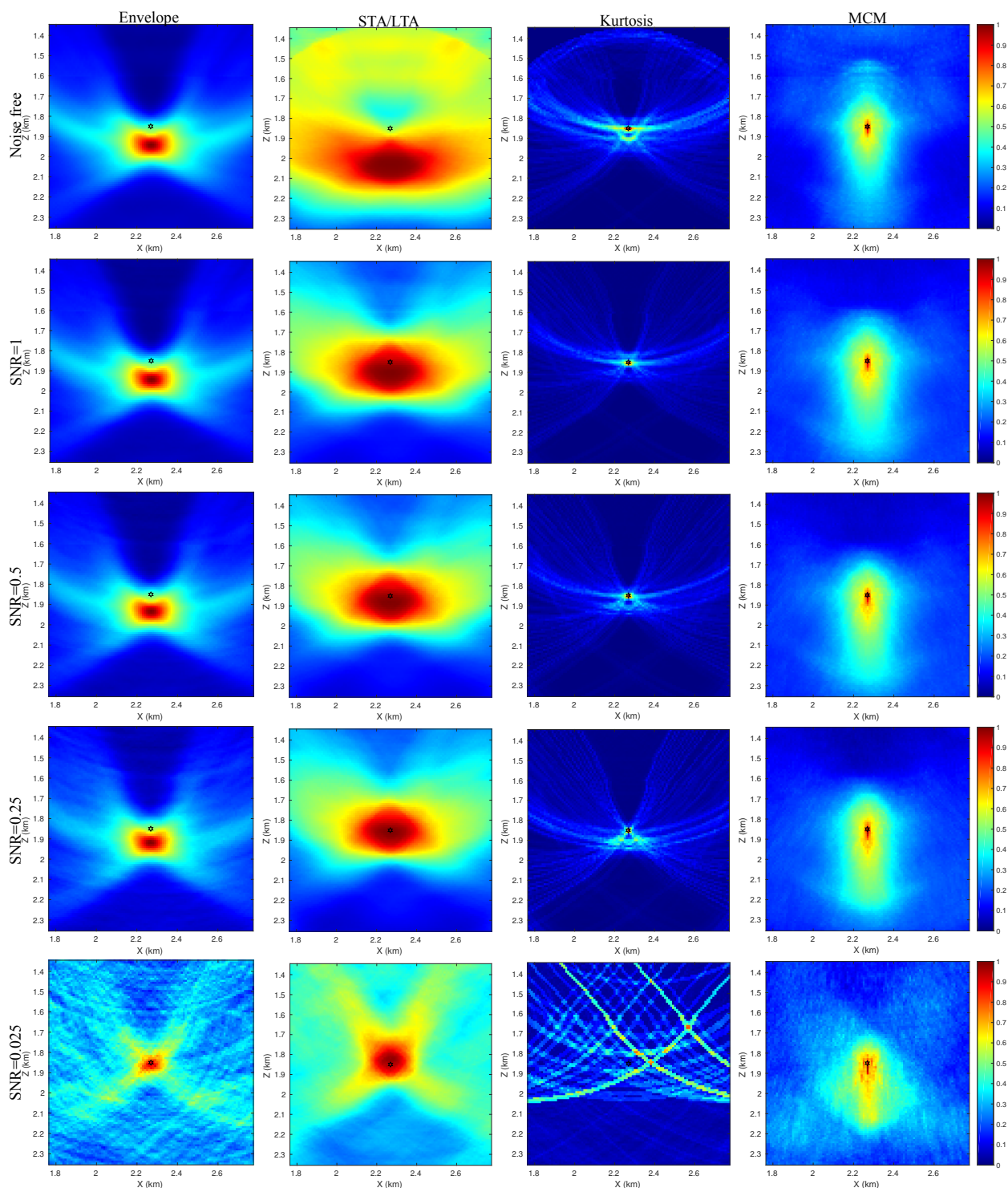


**Figure S.5.** Vertical profiles (XZ profiles) through the true source location of the migration results with automatic quality control scheme (weighting and filtering) under different SNRs. The dark star in the center shows the true source location. The first column shows results of envelope, second column for STA/LTA, third column for kurtosis, fourth column for MCM. The first row shows the results when data is free of noise, second row for SNR is 1, third row for SNR is 0.5, fourth row for SNR is 0.25, fifth row for SNR is 0.025.

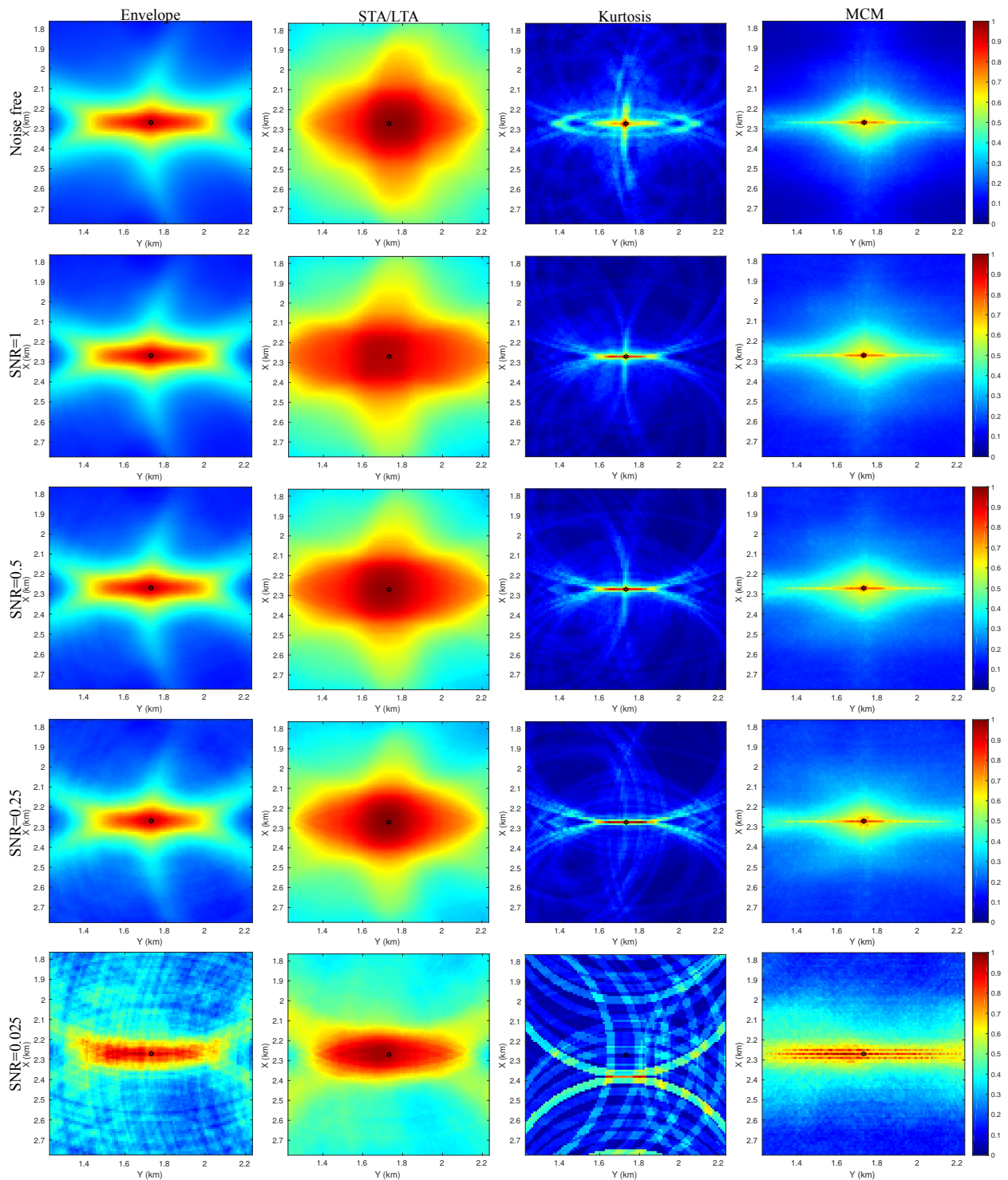


**Figure S.6.** Horizontal profiles (XY profiles) through the true source location of the migration results with automatic quality control scheme (weighting and filtering) under different SNRs. The dark star in the center shows the true source location. The first column shows results of envelope, second column for STA/LTA, third column for kurtosis, fourth column for MCM. The first row shows the results when data is free of noise, second row for SNR is 1, third row for SNR is 0.5, fourth row for SNR is 0.25, fifth row for SNR is 0.025.